

Long-distance Asthenospheric Transport of Plume-influenced Mantle

J. Hua^{1,2}, K. M. Fischer¹, E. Gazel³, E. M. Parmentier¹ and G. Hirth¹

¹ Department of Earth, Environmental and Planetary Sciences, Brown University, Providence, RI 02906, USA

² Department of Geological Sciences, Jackson School of Geosciences, The University of Texas at Austin, Austin, TX, 78712, USA

³ Department of Earth and Atmospheric Sciences, Cornell University, Ithaca, NY, 14853, USA

Corresponding author: Junlin Hua (junlin.hua@austin.utexas.edu)

Key Points:

- Upper mantle partial melting prevails beneath the Anatolian Region
- Plume-originated asthenospheric mantle is transported from East Africa to Anatolia while preserving its elevated temperature
- Transport over ~2500 km is facilitated by reduced viscosity due to high temperature and possibly takes only ~10 Myr

19 **Abstract**

20 The origin of widespread volcanism far from plate boundaries and mantle plumes remains a
21 fundamental unsolved question. An example of this puzzle is the Anatolian region, where
22 abundant intraplate volcanism has occurred since 10 Ma, but a nearby underlying plume
23 structure in the deep mantle is lacking. We employed a combination of seismic and geochemical
24 data to link intraplate volcanism in Anatolia to a trail of magmatic centers leading back to East
25 Africa and its mantle plume, consistent with northward asthenospheric transport of over ~2500
26 km distance. Joint modeling of seismic imaging and petrological data indicates that the east
27 Anatolian mantle potential temperature is higher than the ambient mantle (~1420°C). Based on
28 multiple seismic tomography models, the Anatolian upper mantle is likely connected to East
29 Africa by an asthenospheric channel with low seismic velocities. Along the channel, isotopic
30 signatures among volcanoes are consistent with a common mantle source, and petrological data
31 demonstrate similar elevated mantle temperatures, consistent with little cooling in the channel
32 during the long-distance transport. Horizontal asthenospheric pressure gradients originating from
33 mantle plume upwelling beneath East Africa provide a mechanism for high lateral transport rates
34 that match the relatively constant mantle potential temperatures along the channel. Rapid long-
35 distance asthenospheric flow helps explain the widespread occurrence of global intraplate
36 magmatism in regions far from deeply-rooted mantle plumes throughout Earth history.

37

38 **Plain Language Summary**

39 Volcanoes that exist in the middle of tectonic plates are often thought to be produced by plumes
40 of high temperature mantle that originate deep within the Earth, near the core-mantle boundary.

41 However, while many of these “intraplate” volcanoes share chemical compositions with plume-
42 related volcanism, their close connection to a deep mantle upwelling is not clear for all locations.
43 In this study, we jointly analyze images of the Earth’s interior structure from earthquake waves
44 and the chemical properties of erupted magmas to make the case that: 1) the volcanoes in the
45 Anatolia region are fed by a mantle plume that lies beneath the East African Rift system, and 2)
46 upper mantle is transported horizontally over ~2500 km from Africa to Anatolia without
47 significant cooling. We modelled mantle transport driven by a hot upwelling mantle plume and
48 found that it is fast enough to explain the apparent lack of cooling. These results suggest that
49 mantle plumes can affect a much larger volume of the Earth than is commonly assumed.

50

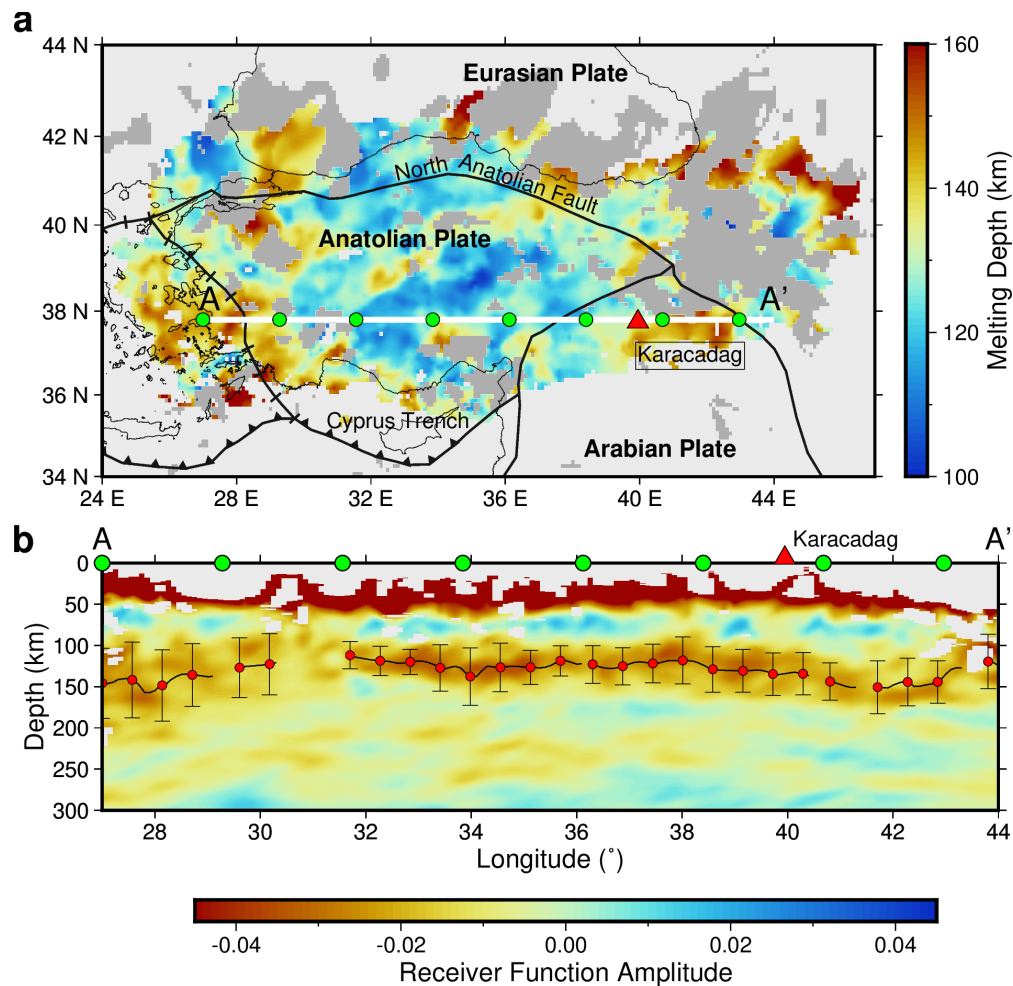
51 **1 Introduction**

52 Intraplate volcanism is widely observed on Earth. Some intraplate volcanoes lie above mantle
53 plumes which potentially bring hot and fertile materials from as deep as the core-mantle boundary
54 to the surface (French & Romanowicz, 2015; Morgan, 1972). These plume-associated volcanic
55 fields often feature chemical compositions that differ from average upper mantle, including
56 elevated source temperatures as well as trace-element and isotopic signatures of recycled and
57 primordial mantle domains (Bao et al., 2022; Herzberg et al., 2007; Hofmann, 2007; Mundl et al.,
58 2017; Putirka, 2005; Trela et al., 2017). However, other intraplate volcanic fields lack a vertical
59 connection to a mantle plume and their origins are debated (Bao et al., 2022; Conrad et al., 2011).

60 To explain intraplate magmatism that is not located near a mantle plume, horizontal asthenospheric
61 flow over distances of ~1000 km or has been proposed in western Africa (Ebinger & Sleep, 1998)
62 and the Iceland-North Atlantic region (Schoonman et al., 2017), and such flow has also been

63 modelled beneath the Pacific Ocean over distances that exceed 2000 km (Ballmer et al., 2013).
 64 However, observationally, uncertainty remains regarding the distances over which material from
 65 a mantle plume can permeate the surrounding asthenosphere and the time-scales over which it
 66 maintains its elevated temperature (Phipps Morgan et al., 1995). This information is critical to
 67 understanding the role of plumes throughout Earth history, including large igneous provinces
 68 where magmas sharing a mantle source erupt over massive areas (Madrigal et al., 2016; Marzoli
 69 et al., 1999; Stern et al., 2020), and on planets like Venus that lack moving tectonic plates (Smrekar
 70 et al., 2010).

71



72

73 **Figure 1.** Constraints on seismic velocity gradients and melting onset depths from Sp receiver
74 functions. (a) Melting onset depths in Anatolia inferred from the positive mantle velocity gradient
75 at depths of 100-160 km observed in the Sp common conversion point stack. Colors show positive
76 velocity gradient depths; dark gray regions lack a clear observation of this feature. Profile A-A'
77 location shown by white line with green circles. The Karacadag volcanic field is labelled by the
78 red triangle, and thick black lines show plate boundaries (Bird, 2003). Subduction boundaries are
79 labeled with triangles and divergent boundaries with bars. (b) Sp receiver function common
80 conversion point stack amplitude for profile A-A' (10-100 s bandpass filter). Positive velocity
81 gradient depths picked from the stack are shown by red circles. Error bars (black lines) are the
82 depth ranges spanned by the Sp phase from this gradient, estimated as three times the standard
83 deviation of the receiver function amplitude distributions (e.g. Figure S1a). Positive amplitudes
84 (blue) at depths of 50-90 km represent the lithosphere-asthenosphere boundary. Green circles
85 correspond to markers in (a).

86

87 In this paper, we address these fundamental questions by exploring the source of intraplate
88 magmatism in Anatolia and its connection to lower mantle plumes. The tectonically active
89 Anatolian region lies at the northeast edge of the Mediterranean Sea (Figure 1a). To the north, the
90 Anatolian plate is separated from the Eurasian plate by the North Anatolian Fault; to the south, the
91 African plate subducts beneath Anatolia via the Cyprus trench; and to the southeast, the Anatolian
92 plate is compressed by the Arabian plate (Bird, 2003).

93 Extensive intraplate volcanism exists in Anatolia, and while the erupted basaltic magmas have
94 indicated mantle temperatures and compositions similar to hotspot volcanoes in some areas
95 (McNab et al., 2018; Nikogosian et al., 2018; Reid et al., 2017), this region lacks evidence for a
96 mantle plume that is locally connected to the lower mantle (French & Romanowicz, 2015; Lei et
97 al., 2020). To explain the intraplate magmatism, regional processes within Anatolia have been
98 proposed, including upwelling related to lithospheric extension, lithospheric delamination, and
99 slab rollback and/or fragmentation (e.g. Delph et al., 2017; Göğüş & Pysklywec, 2008; Keskin,
100 2007; Lynner et al.; Memiş et al., 2020). Although these processes dramatically alter the
101 lithosphere, in most cases they do not result in broad zones with significantly hotter asthenosphere

102 and elevated mantle potential temperatures, although local temperature increases of tens of degrees
103 may be produced (e.g. King & Ritsema, 2000; Van Wijk et al., 2008). Alternatively, other studies
104 have proposed that hot mantle derived from upwelling beneath the East African Rift (EAR) flows
105 horizontally over thousands of kilometers towards Anatolia (Ershov & Nikishin, 2004; Faccenna
106 et al., 2013; Hansen et al., 2012; Wei et al., 2019). This model is consistent with regional seismic
107 velocity and anisotropy patterns (Wei et al., 2019), and also local seismic tomography results (e.g.
108 Berk Biryol et al., 2011) that suggest that hot mantle material could flow into the Anatolian region
109 through the slab window opened by the Arabian plate-Anatolian plate collision. This type of model
110 provides a possible explanation for high mantle potential temperatures beneath Anatolia. Once in
111 Anatolia, this hotter-than-average asthenosphere could interact with regional processes such as
112 lithospheric extension, delamination, and slab roll-back and break-off.

113 To systematically test the plausibility of long-distance transport, several questions must be
114 addressed: 1) What are the bounds on mantle potential temperature beneath Anatolia and are they
115 indeed in the range of hotspot regions globally? 2) Does mantle along the transport path record a
116 common mantle source? 3) Is the estimated mantle temperature along the transport path consistent
117 with a single, plume-related, heat source? 4) With reasonable mantle viscosities, is the long-distant
118 transport consistent with constraints from geodynamic models?

119 In the following sections, we address these questions by joint interpretation of seismic,
120 petrological, and geochemical data, aided by geodynamical modeling, to make the case that rapid
121 lateral transport of high temperature plume-derived asthenosphere from the EAR to Anatolia is
122 possible. To answer question (1), in Section 2 we used novel joint modeling of seismic receiver
123 function phases and basaltic primary magma equilibration conditions to explain the extensive
124 upper mantle melting beneath Anatolia and to constrain upper mantle potential temperature. To

125 answer question (2), in Section 3 we analyzed multiple seismic tomography models to verify that
126 they are consistent with a channel of high-temperature asthenosphere, and we compared various
127 radiogenic isotope ratios along the transport route. To answer question (3), in Section 4, we
128 obtained mantle potential temperatures at different locations along the path with basaltic magma
129 samples. Finally, to answer question (4), in Section 5, we used a simplified 1D pressure-driven
130 Poiseuille flow model to demonstrate the physical plausibility of rapid long-distance
131 asthenospheric transport.

132

133 **2 Anatolian Mantle Temperatures**

134 2.1 Extensive Partial Melting Beneath Anatolia

135 The Anatolian upper mantle has recently been imaged with Sp receiver function common-
136 conversion point stacking using a new approach that incorporates Sp sensitivity kernels in the
137 spatial functions used to weight the receiver functions as they are summed at each point in the
138 stack (Hua, Fischer, Wu, et al., 2020). The stacking used 23,787 individual receiver functions.
139 Within the upper mantle, in addition to the commonly observed negative velocity gradient
140 (positive receiver function amplitude) that represents the seismic lithosphere-asthenosphere
141 boundary (LAB) (e.g. Figure S1i), the receiver function stack reveals an unusual and widespread
142 asthenospheric positive shear velocity gradient (PVG) at depths of 100-150 km (Figure 1b & S1)
143 that is indicated by negative receiver function amplitudes. To study the depth range over which
144 this gradient extends, similar stacking of Sp receiver functions was performed using seismograms
145 from a range of bandpass filters. This analysis demonstrated that this velocity gradient is gradual
146 in depth (it extends over more than 30 km) and is better characterized with long-period data (Hua,

147 Fischer, Wu, et al., 2020). Hence, in this study, we used stacks from seismograms with a 10-100 s
148 bandpass filter to study the PVG. The shallower negative velocity gradient (positive receiver
149 function amplitude) associated with the LAB is observed at ~70 km depth (Figure S1) (Hua,
150 Fischer, Wu, et al., 2020). However, due to the thin mantle lithosphere, this phase is clearer at
151 shorter periods (Hua, Fischer, Wu, et al., 2020), so we used stacks from a 2-20 s filter to study this
152 receiver function phase.

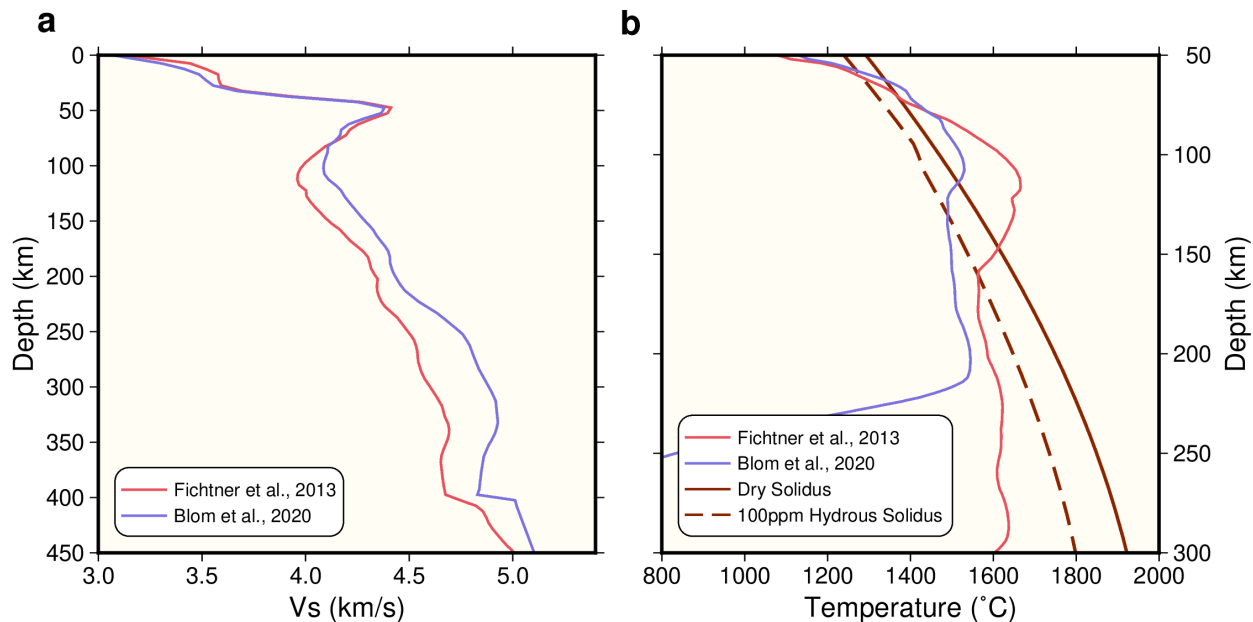
153 To quantify the depths of the PVG and LAB, these receiver function phases were picked with an
154 algorithm (Hua et al., 2018, see Supporting Information Text S1 for details) that assumes the phase
155 amplitude at a given depth is proportional to the probability that the velocity gradient is located at
156 that depth (Figure S1a). This assumption is reasonable given that the common-conversion point
157 stacked receiver function amplitude is proportional to the intensity of the velocity gradient (Hua,
158 Fischer, Mancinelli, et al., 2020). The depth of the phase is defined as the expected depth for the
159 distribution, and the depth extent of the phase is characterized by one and half the standard
160 deviation of the distribution. The phase depth picking indicates that the PVG is present primarily
161 at depths of 100-150 km beneath most of the Anatolian region (Figure 1a), while the LAB phase
162 exists mainly at depths of 60-85 km (Figure S1h).

163 To assess the potential origins of the PVG, we compared its depth to two full-waveform
164 tomography models (Blom et al., 2020; Fichtner et al., 2013). Both velocity models contain a
165 widespread layer of low seismic velocity above the 100-150 km depth of the receiver function
166 PVG, consistent with an interpretation where the PVG is a depth-localized lower boundary to this
167 layer (Hua, Fischer, Wu, et al., 2020). This result is illustrated in Figure 2a for the location of the
168 Karacadag volcanic field. To assess whether partial melt could exist within the low velocity layer,
169 the velocity models were transformed to temperature assuming different mantle conditions and

170 transform relationships (see Supporting Information Text S2). For the case shown in Figure 2, the
171 velocity models were converted to temperature based on the relationship in Yamauchi and Takei
172 (2016) and the shear modulus from Priestley and McKenzie (2013) assuming 100 wt. ppm water
173 in the mantle (Figure 2b), but the direct effects of an unconstrained melt fraction on velocity are
174 not accounted for in the calculation. Temperatures exceed the inferred mantle solidus over most
175 of the low velocity layer, starting at depths of 120-160 km and continuing to depths of 50-60 km.
176 In this depth range, calculated temperatures reach unrealistically high values. However, at supra-
177 solidus conditions, the presence of partial melt will likely also reduce shear wave velocity,
178 resulting in more reasonable mantle temperatures. We tested this result using different mantle
179 conditions as well as a different velocity-temperature relationship (Jackson & Faul, 2010). While
180 these cases result in different estimated mantle temperatures (Figure S2), the estimated geotherm
181 consistently starts to exceed the solidus at depths close to where the PVG is observed, and
182 unrealistically high mantle temperatures are calculated above these depths (Figure S2). Overall,
183 these comparisons overall support the conclusion that the PVG could represent the base of a layer
184 containing partial melt and lies at the depth where the upper mantle starts to melt. The LAB phase
185 is consistent with a negative velocity gradient at the top of this melt-bearing layer.

186 We emphasize that the calculated temperature profiles are highly dependent on the chosen
187 conversion relationship between shear wave velocity and temperature and assumptions about other
188 mantle parameters such as water content (Figures 2 and S2). We therefore do not use this type of
189 velocity-temperature scaling to infer mantle temperatures for the remainder of this paper. Rather,
190 we have developed a new approach, described in the next two sections, which relies on the depths
191 of the PVG and LAB phases and constraints on mantle temperatures from the major element
192 compositions of erupted basalts.

193



194

195 **Figure 2.** V_S -temperature conversion for two velocity models. These examples demonstrate that
 196 the positive velocity gradient at depths of 100-150 km indicated by the Sp phases can be interpreted
 197 as the lower boundary of a layer containing partial melt. However, these loosely constrained
 198 converted temperatures are not used otherwise in our analysis. (a) 1D V_S profiles from local
 199 (Fichtner et al., 2013) and regional (Blom et al., 2020) models at 38.9°N, 33.2°E. (b) Temperature
 200 converted from V_S in (a); cases for a dry and 100 wt. ppm hydrous solidus (Hirschmann et al.,
 201 2009) are shown by solid and dashed dark red lines. Conversions are based on the V_S -temperature
 202 relationship from Yamauchi and Takei (2016), assuming 100 wt. ppm of mantle water, and the
 203 modulus estimated based on Priestley and McKenzie (2013).

204

205 2.2 Primary Magma Equilibration Pressure and Temperature (P-T) Conditions

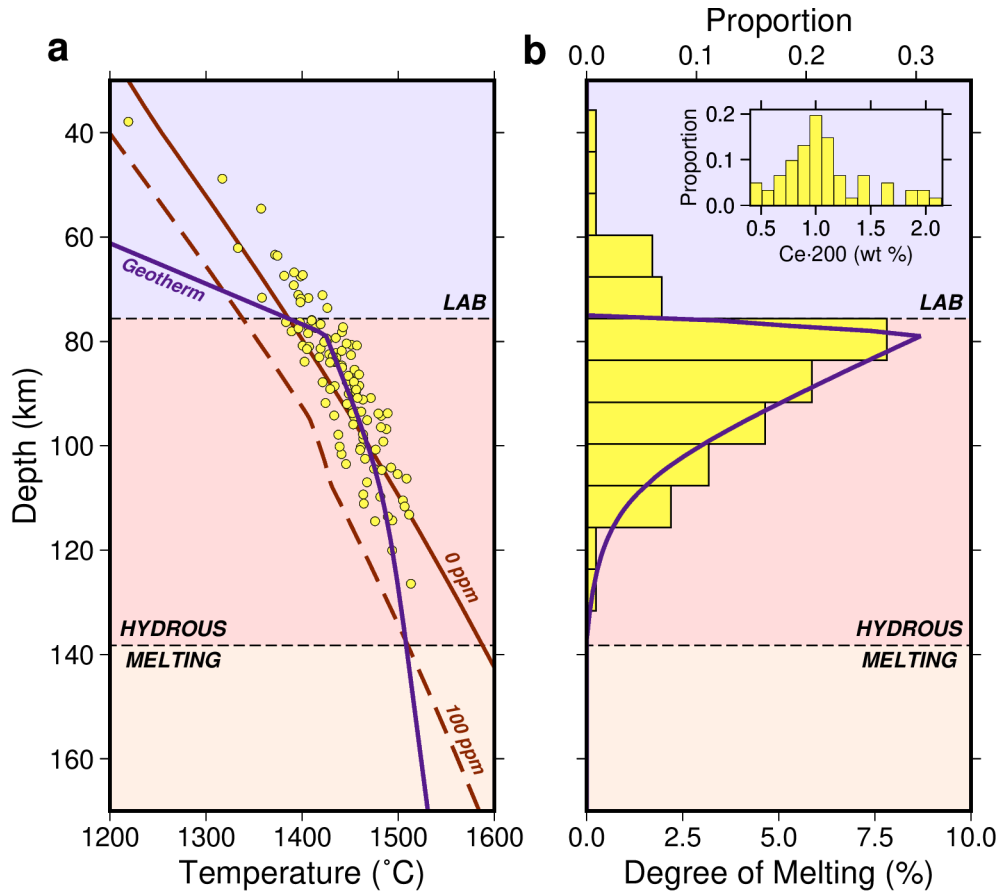
206 To provide independent constraints on the mantle geotherm from major element compositions of
 207 erupted basalt samples, we first picked reliable basalt samples from the Karacadag volcanic field
 208 (Figure 1a). We also estimated the temperatures and pressures of last mantle equilibration from
 209 basalts in other Anatolian volcanic fields, but the Karacadag field was the only location where a
 210 sufficient number of asthenospheric samples were found. In this study, all samples in the
 211 GEOROC database till 2020 (<http://georoc.mpch-mainz.gwdg.de/Georoc>) from 37° to 38°N and

212 39° to 40.5°E were classified as being from Karacadag (Supporting information Data Set S1).
213 The FeO and Fe₂O₃ weight percentages were first converted to FeO_{total} to represent the total iron
214 weight percentage. Then we calculated the sum of the weight percentages for major elements,
215 and only samples with summed weight percentage between 98% and 102% were used. For these
216 samples, the major element weight percentages were normalized to make their sum equal to
217 100%. We only used samples that follow an olivine control trend based on major element (FeO,
218 TiO₂, CaO, Al₂O₃, CaO/Al₂O₃, Na₂O, etc.) variations with MgO, and limiting the samples to
219 those with MgO higher than 8 wt. %, and SiO₂ higher than 45 wt. % to be consistent with
220 experiments done with peridotite sources that are the basis for modeled primary magmas FeO-
221 MgO thermometers (Herzberg & Asimow, 2008; Lee et al., 2009). The average location for the
222 117 selected samples is 37.58°N, 39.83°E. The Sp PVG phase at this location (Figure S1a) is
223 centered at 138 km depth with a phase depth extent of 28.5 km (defined as 1.5 times the
224 distribution standard deviation), as obtained from the receiver function phase picking.

225 Primary magma equilibration pressure-temperature (P-T) conditions for the basaltic magma
226 samples were calculated based on the Lee et al. (2009) parameterization (Figure 3a). Starting from
227 the major element compositions of the collected melt samples, this method first adds olivine
228 increments in equilibrium with the instantaneous melt composition back to the melt until the melt
229 reaches equilibration with the suggested ambient mantle composition (explaining why only
230 samples in an olivine control trend can be used); the corresponding melt composition represents
231 the primary magma. Then, the primary magma equilibration P-T conditions are estimated from the
232 primary magma major element compositions using an experimentally-defined empirical
233 relationship (Lee et al., 2009). A more recently calibrated empirical relationship also exists (Plank
234 & Forsyth, 2016), based on the same experimental data used by Lee et al. (2009); the resulting T-

235 P estimates are similar (Plank & Forsyth, 2016). We therefore chose to continue using the well-
 236 established thermobarometer in Lee et al. (2009).

237



238

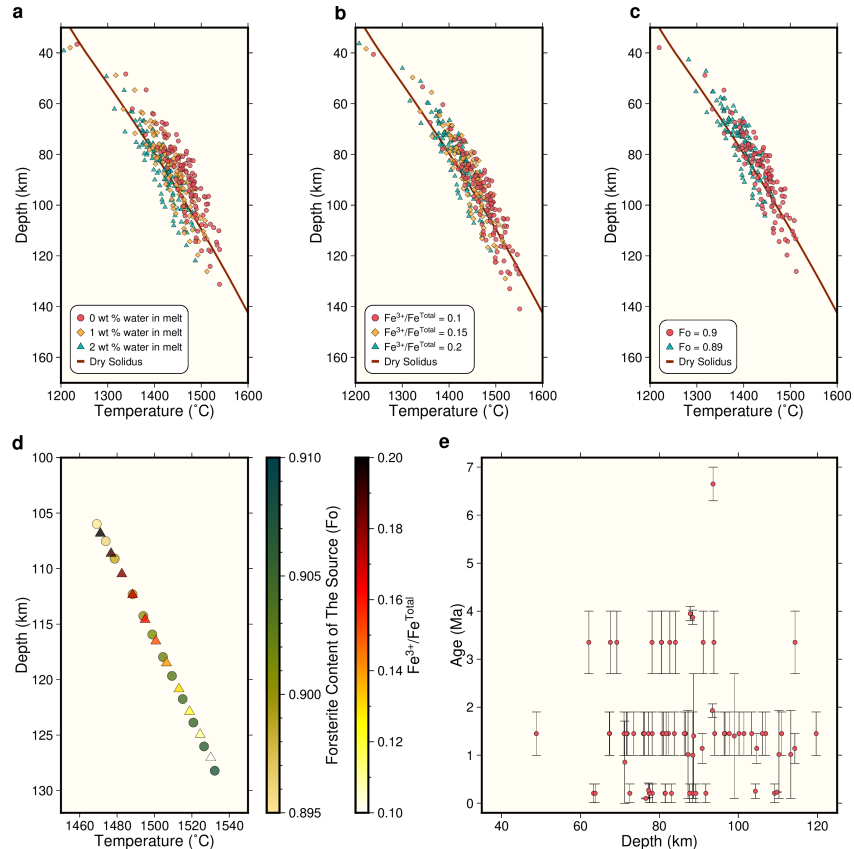
239 **Figure 3.** Mantle T_P determination with Karacadag samples. (a) The geotherm (purple line) that
 240 best fits primary magma equilibration P-T conditions (yellow dots) and melting onset depth from
 241 the Sp stack (lower black dashed line) beneath the Karacadag volcanic field. The dry solidus and
 242 100 wt. ppm water solidus (Hirschmann et al., 2009) are shown by the red solid and dashed lines.
 243 The upper dashed line indicates the lithosphere-asthenosphere boundary from the Sp stack. (b)
 244 Degree of melting predicted for the mantle conditions in (a) (purple line). The vertical histogram
 245 shows the distribution of basalt sample equilibration depths. The histogram in the inset shows the
 246 distribution of 200 times Ce for samples as a proxy for water in the melt sample.

247

248 The estimated final P-T equilibration conditions also depend on the assumed water weight
 249 percentage in the melt sample, oxidation state (represented by Fe^{3+}/Fe^{Total}) and source mantle
 250 forsterite content (Fo) (Figure 4a-4c). We assumed the 1 wt. % water in the melt, a typical value

251 for primitive intraplate basalts (Dixon & Clague, 2001; Plank & Forsyth, 2016). This value is also
 252 in the range of water contents in olivine hosted melt inclusions that were collected at a volcano
 253 ~300 km away from Karacadag (Özdemir et al., 2011). To further validate the assumed water
 254 content, the Ce abundances of these basalt samples were used as a proxy (Dixon et al., 2002). Ce
 255 values were multiplied by 200 (Dixon et al., 2002) to obtain the estimated water content (inset in
 256 Figure 3b), which is also distributed around 1 wt. %. If the actual water in the melt is not
 257 approximately the assumed value, this parameter could introduce a ~30°C difference in the
 258 calculated mantle equilibration temperature (e.g. Figure. 4a). For the other two factors, the effects
 259 from $\text{Fe}^{3+}/\text{Fe}^{\text{Total}}$ and Fo are nearly identical (Figure 4d), so we fixed Fo to be 90% and only solved
 260 for bounds on the value of $\text{Fe}^{3+}/\text{Fe}^{\text{Total}}$.

261



262

263 **Figure 4.** Primary magma equilibration P-T conditions for Karacadag samples. In (a)-(c), we test
264 the effect of wt. % water in melt, $\text{Fe}^{3+}/\text{Fe}^{\text{Total}}$ and Fo on the estimated melt equilibration conditions.
265 Red lines in (a)-(c) show the dry solidus (Hirschmann et al., 2009). (a) The equilibration conditions
266 with varying water in the melt (labelled in legends); shifts in temperature are larger than shifts in
267 pressure. (b) The equilibration conditions with varying oxidation state ($\text{Fe}^{3+}/\text{Fe}^{\text{Total}}$); shifts in
268 pressure are larger than shifts in temperature. (c) The equilibration conditions with different
269 forsterite content (Fo). (d) The effect of changes in Fo and $\text{Fe}^{3+}/\text{Fe}^{\text{Total}}$ on the equilibration
270 conditions for a single sample (Sample ID 3983 in Supporting Information Data Set S1). (e)
271 Equilibration depth versus sample age for the estimated and assumed parameters (1 wt. % water
272 in melt, Fo equal to 0.9 and $\text{Fe}^{3+}/\text{Fe}^{\text{Total}}$ equal to 0.1615). Error bars show age uncertainties from
273 published studies.

274

275 To constrain $\text{Fe}^{3+}/\text{Fe}^{\text{Total}}$, we used the depth of the smoothed Sp receiver function LAB phase
276 (Figure S1h). $\text{Fe}^{3+}/\text{Fe}^{\text{Total}}$ primarily affects the estimated equilibration pressure but also has a
277 smaller effect on equilibration temperature (Figure 4b). Assuming the equilibration P-T conditions
278 represent the geotherm, the distribution of the sample equilibration depths should be similar in
279 shape to variation in the degree of melting with depth, as depths with a higher degree of melting
280 are more likely to have generated melt that is extracted to the surface and collected, especially for
281 a volcanic field with an abundant number of samples in a small region like Karacadag. Since the
282 LAB phase represents the upper boundary of the low velocity layer in which partial melt is
283 expected to be concentrated, the degree of melting is expected to increase abruptly with depth
284 across the seismically defined LAB, so we expect the number of samples equilibrated beneath the
285 LAB depth to be much greater than the number equilibrated above this depth. In practice, we
286 performed a grid search over $\text{Fe}^{3+}/\text{Fe}^{\text{Total}}$ values from 0.05 to 0.3 with an interval of 0.001 to find
287 the $\text{Fe}^{3+}/\text{Fe}^{\text{Total}}$ values that result in the largest difference between the number of samples in the 10
288 km depth range beneath the LAB (75-85 km depth) and the number of samples in the 10 km depth
289 range above the LAB (65-75 km depth) (Figure 3b). The 10 km interval is used as it is the standard
290 deviation of the picked LAB depth distribution for this region. Since $\text{Fe}^{3+}/\text{Fe}^{\text{Total}}$ values between
291 0.16 and 0.163 produce the maximum difference in number of samples equilibrated above and

292 below the LAB depth, we set $\text{Fe}^{3+}/\text{Fe}^{\text{Total}}$ to 0.16 for the remaining analyses. This value is
293 consistent with high temperature upper mantle conditions, as shown by samples from other
294 intraplate locations like Hawaii and Iceland that also indicate similar $\text{Fe}^{3+}/\text{Fe}^{\text{Total}}$ values
295 (Moussallam et al., 2019).

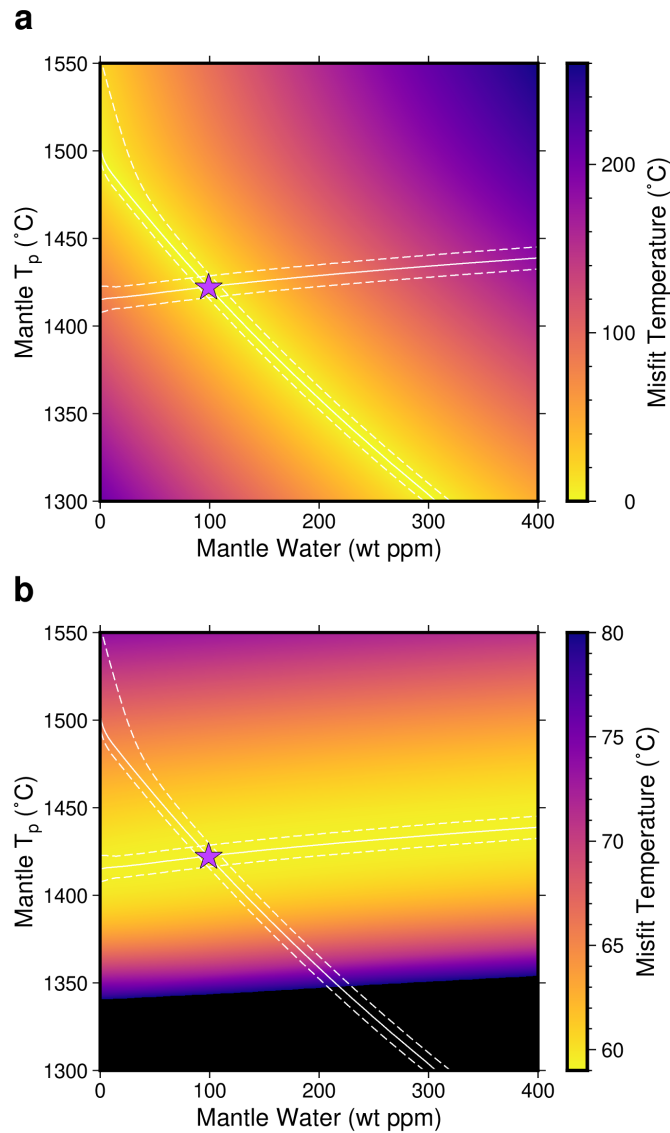
296 With these parameters, we calculated the equilibration P-T conditions of the Karacadag melt
297 samples (Lee et al., 2009) (Supporting Information Data Set S1). To convert equilibration
298 pressures to depths, we used the pressure-depth relationship obtained in the V_S -temperature
299 conversion section assuming the local velocity model (Fichtner et al., 2013) for 70 s, a mantle with
300 100 wt. ppm of water, the V_S -temperature relationship of Yamauchi and Takei (2016), and the
301 shear modulus dependence of Priestley and McKenzie (2013) (Supporting Information Text S2).

302

303 2.3 Joint Modeling of Receiver Function and Primary Magma Equilibrium Conditions

304 With both the Karacadag melting onset depth at 138 km from the Sp receiver function PVG phase
305 and the estimated primary magma equilibration P-T conditions from the 117 reliable Karacadag
306 basalt samples, both the mantle potential temperature (T_P) and the water content of the Karacadag
307 volcanic field are constrained through joint modeling. We first assumed that the primary magma
308 P-T conditions represent the actual mantle conditions, and the asthenospheric geotherm follows an
309 adiabat. Values of T_P and mantle water content were then obtained by requiring that the
310 corresponding mantle geotherm approximates the equilibration P-T conditions, and that the
311 geotherm intersects the hydrous solidus for the given water content (Hirschmann et al., 2009) such
312 that the onset of melting matches the seismically-observed (PVG) melting depth (Figure 3a).

313



314

315 **Figure 5.** Joint modeling results of Sp-based melting onset depth and basalt equilibration P-T
 316 conditions. Misfit values are shown as colored surfaces for (a) melting depths and (b) basalt
 317 sample P-T values. White solid lines show T_P and water content values that result in minima for
 318 both misfit functions, and white dashed lines show twice the standard deviation for the solid lines.
 319 The purple star shows the best fitting T_P and water content values for Karacadag samples. Black
 320 regions have misfits beyond the upper limit of the color bar.

321

322 In practice, a grid search of T_P and mantle water content values was employed for the modeling

323 (Figure 5). We tested T_P from 1300 $^{\circ}\text{C}$ to 1550 $^{\circ}\text{C}$, and water from 0 to 400 wt. ppm. For each tested

324 T_P -water combination, we estimated two misfits between model predictions and conditions based

325 on either the observed melting depth from the Sp stack or the basalt samples. One misfit is
326 $|T_{soli} - T_{geo}|$ (Figure 5a), where T_{soli} is the hydrous solidus temperature at the observed melting
327 depth from the PVG with the assumed water content, and T_{geo} is the predicted geotherm
328 temperature at the same depth for the values of T_P and water (see Supporting Information Text S3
329 for how we construct geotherms). The misfit between the predicted geotherm and the basalt
330 equilibration P-T conditions is characterized as $\|T_{sample} - T_{geo}\|_2$ (Figure 5b), where in this L2-norm
331 misfit function, T_{sample} represents the primary magma equilibration temperature at its equilibration
332 depth, while T_{geo} represents the predicted geotherm temperature at that equilibration depth. Each
333 of the misfit functions reaches a minimum value along a curve that reflects trade-offs in the effects
334 of T_P and water (Figure 5). However, the intersection of the two misfit minima curves resolves
335 the T_P and water conditions that satisfy both seismic and basalt data. The best-fitting values for the
336 Karacadag basalts are 1420°C for T_P and 100 wt. ppm for mantle water content.

337 To further test the estimated values of T_P and mantle water content, we predicted the degree of
338 melting for the inferred geotherm (Hirschmann, 2010; Hirschmann et al., 2009; Katz et al., 2003)
339 (see Supporting Information Text S3). The predicted degree of melting correlates with the
340 observed equilibration depth distribution of the basaltic samples (Figure 3b). Since melt is more
341 likely to be extracted at depths with higher degrees of melting, this agreement validates the T_P and
342 mantle water content estimates and the assumption that P-T conditions represent the geotherm. An
343 alternative interpretation for the equilibration P-T values from the basalts is that they always
344 represent re-equilibration of the magmas at the base of the lithosphere (Gazel et al., 2012b; Plank
345 & Forsyth, 2016), and that the distribution of equilibration depths (Figure 3b) is caused by

346 lithospheric thinning. However, this interpretation requires that magma samples equilibrated at
347 shallower depths be younger than those from deeper depths, which is not evident in the basalt data
348 (Figure 4e).

349

350 2.4 The Uncertainty of the Calculated Mantle Conditions

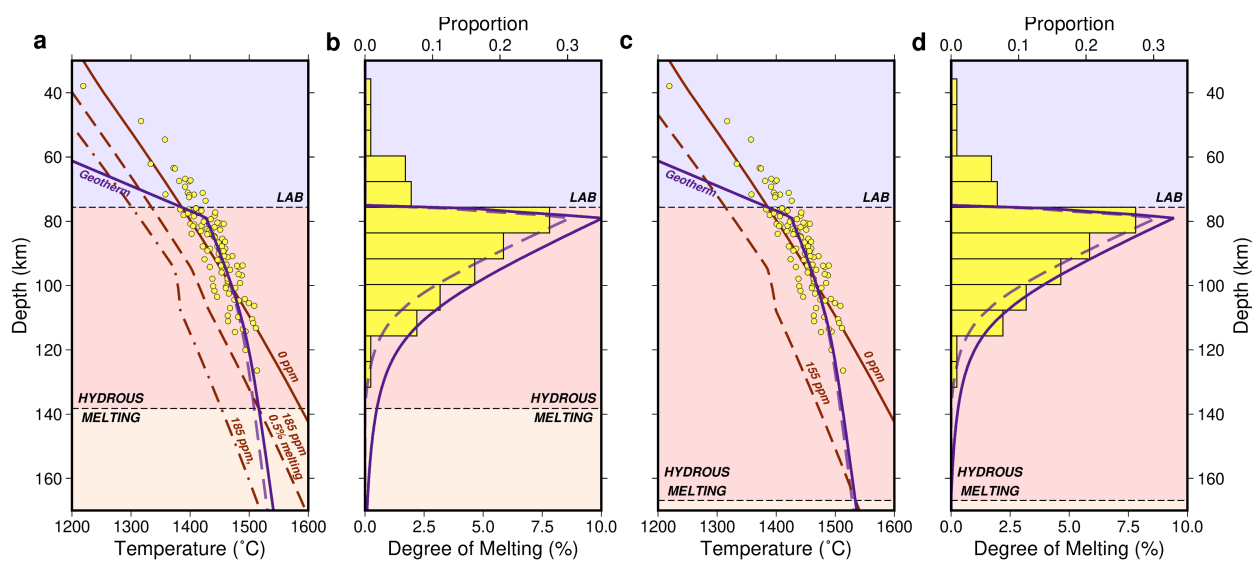
351 We quantified the uncertainty of our grid search method for determining T_P and mantle water
352 content. For uncertainties related to the seismically-inferred melting onset depth, a Monte Carlo
353 method was used. Since the melting onset depth is defined as the center of the receiver function
354 PVG phase, to calculate its uncertainties we randomly perturbed the stacked S_p receiver function
355 at Karacadag based on an estimated covariance matrix, whose elements represent the covariance
356 between receiver function amplitudes at different depths. This operation was repeated 60,000
357 times, and the picked depth of the perturbed receiver function PVG phase was recorded. We used
358 twice the standard deviation of the 60,000 PVG depths as the PVG depth uncertainty (± 9.7 km).
359 To construct the covariance matrix used in this operation, the variance of the S_p stacked amplitudes
360 at Karacadag (Hua, Fischer, Wu, et al., 2020) was used to form the diagonal terms. The off-
361 diagonal terms, which reflect the covariance between different depths, were based on the Gaussian
362 shape functions that were used in the time-domain deconvolution of the receiver functions; these
363 Gaussians have a standard deviation equal to the S-wave wavelength at 1 s (Hua, Fischer, Wu, et
364 al., 2020). The PVG depth uncertainty (± 9.7 km) was transferred to the uncertainty of the melting
365 depth trade-off curve in Figure 5. For the uncertainty related to the basalt samples, we bootstrapped
366 the 117 samples 500 times. Each time the corresponding trade-off curve was recorded, and twice
367 the standard deviation of that curve was used as its uncertainty (Figure 5).

368 Based on the uncertainties in the seismically-constrained melting depth and the basalt sample
369 trade-off curves, the resulting estimates of T_P and mantle water content have two-standard
370 deviation uncertainties of $\pm 6.4^\circ\text{C}$, and ± 17 wt. ppm. The resulting T_P value of $1420 \pm 6.4^\circ\text{C}$ for the
371 Karacadag field is consistent with the 1420°C T_P estimate from Reid et al. (2017), obtained with
372 a different method. It also falls within the range of elevated T_P values for eastern Anatolia from a
373 previous study (McNab et al., 2018). However, our calculated uncertainties depend strongly on
374 our interpretation of the PVG phase, i.e. that the center of the phase represents the melting onset
375 depth. In addition, the depth uncertainty of 9.7 km represents the uncertainty of the picked center
376 of the PVG phase, which is different from the previously described PVG depth extent. The latter
377 is represented by 1.5 times the standard deviation of the receiver function amplitude distribution
378 (28.5 km, Figure S1a) where the receiver function amplitudes are treated as the probability
379 distribution for the depth of the PVG phase. Similarly, the bootstrapping result for the geotherm
380 determined from the basalt samples represents the uncertainty for the representative geotherm that
381 is closest to all of the samples. However, if geotherms that pass through calculated equilibration
382 conditions for each individual sample are considered, their variation would be much bigger (as
383 evident from the spread of samples in Figure 3a).

384 To make sure the temperature estimation is not biased by our interpretation of the observed Sp
385 receiver function PVG phase, we also tested two alternative scenarios. In the first scenario, we
386 considered the possibility that the depth of the center of the PVG phase corresponds to 0.5% of
387 melting instead of incipient melting (Figure 6a & 6b) since a small amount of melt could be present
388 at greater depths due to CO_2 (Dasgupta et al., 2007). The joint modeling in this case produces a
389 T_P of 1430°C and a water content of 185 wt. ppm. In the second scenario, we assumed that the
390 lower boundary of the positive velocity gradient Sp phase was taken as the melting onset depth.

391 In other words, the center depth of the phase plus the depth extent (1.5 times standard deviation
 392 for the PVG phase distribution 28.5 km) was assumed to define the melting onset depth (Figure 6c
 393 & 6d). This case yields a T_P of 1425°C and a water content of 155 wt. ppm. Overall, both cases
 394 introduce little change in T_P estimation but have a larger effect on inferred values of mantle water
 395 content.

396



397

398 **Figure 6.** Alternative scenarios for mantle T_P determination for Karacadag. (a)/(b) The scenario
 399 where the positive velocity gradient S_p phase represents 0.5% of melting (Hirschmann, 2010)
 400 instead of incipient melting, and 185 wt. ppm water is the best-fitting value. a) The solid purple
 401 line shows the final determined geotherm that best fits primary magma equilibration P-T
 402 conditions (yellow dots) and melting onset depth from the S_p stack (lower black dashed line)
 403 beneath the Karacadag volcanic field. The dashed red line shows the 185 wt. ppm mantle
 404 0.5% melting conditions, and the dotted dashed line shows the 185 wt. ppm hydrous solidus. b)
 405 Degree of melting predicted for the mantle conditions in (a) (purple line). The vertical histogram
 406 shows the distribution of basalt sample equilibration depths. (c)/(d) The scenario where the bottom
 407 of the positive velocity gradient is the melting depth, and 155 wt. ppm water is the best-fitting
 408 value. The solid purple line shows the final determined geotherm (c) and degree of melting (d). In
 409 (c), the dashed red line shows the 155 wt. ppm hydrous solidus. Otherwise, these plots are similar
 410 to Figure 3 except without the inset C_e histogram, and with additional purple dashed lines that
 411 show the geotherm or degree of melting which are the solid purple lines in Figure 3.

412

413

414 2.5 Mantle Conditions beneath other Regions of Anatolia

415 Mantle T_P values were also estimated for other regions of Anatolia. We first assumed the solidus
416 for a mantle source with 100 wt. ppm of water (Hirschmann et al., 2009), consistent with our
417 analyses of the Karacadag basalts with the assumption that the center of the PVG defines the
418 melting onset depth (Figure 3). Then we determined T_P across the region by requiring that its
419 corresponding geotherm intersects the solidus at the depth of the local seismically-determined
420 PVG, again associated with the onset of mantle melting. The resulting T_P distribution for Anatolia
421 ranges from 1350°C to 1450°C (Figure S3a).

422 To further illustrate that T_P estimates are relatively insensitive to how the PVG phase is interpreted,
423 Anatolia-wide T_P values were also calculated using scenarios where the PVG corresponds to 0.5%
424 of melt (Figure 6a and 6b) or that melting starts at the lower bound on PVG depth (Figure 6c and
425 6d), while assuming the previously-determined water contents beneath Karacadag for these
426 scenarios (185 wt. ppm and 155 wt. ppm, respectively). The resulting T_P maps are similar to those
427 calculated assuming that the center of the PVG defines the melting onset depth (Figure S3). These
428 results show that although the estimated water content depends strongly on how we interpret the
429 PVG phase, since the mantle T_P is mainly constrained by the basalt samples, its value is not
430 strongly influenced by the choice of PVG interpretation. However, since mantle water content is
431 not directly constrained in the Anatolia-wide T_P maps, we base the following analyses related to
432 elevated Anatolian temperatures on the well-constrained value of $1420 \pm 6.4^\circ\text{C}$ beneath Karacadag.

433

434 2.6 Mantle Conditions beneath Karacadag Relative to Ambient Mantle

435 Based on Herzberg and Gazel (2009), the T_P of normal ambient mantle ranges from 1300°C to
436 1400°C. If we use the set of adiabat-related parameters used in that study (Iwamori et al., 1995),
437 the estimated T_P in Karacadag would be 1435°C, higher than the value of 1420°C that is based
438 on parameters from Katz et al. (2003) we used here. Therefore, Karacadag is at least ~35°C
439 hotter than the upper bound for a normal ambient mantle. The Karacadag T_P does overlap the
440 higher end of the mid-ocean ridge T_P ranges of some previous studies (Bao et al., 2022; Courtier
441 et al., 2007; Dalton et al., 2014; Putirka, 2008). However, differences in T_P measurement
442 methods make it difficult to directly compare the Karacadag T_P values to some of these studies,
443 e.g. the T_P values inferred from seismic velocities in Bao et al. (2022). In addition, when
444 determining ambient mantle T_P ranges, the use of basalt samples that are close to active mantle
445 plumes or do not lie on an olivine control trend would obscure ambient mantle conditions
446 (Herzberg & Asimow, 2008; Herzberg et al., 2007; Madrigal et al., 2016). Hence, we choose to
447 put more weight on the comparison of the Karacadag T_P values to Herzberg and Gazel (2009),
448 where accounting for differences in T_P estimation is straightforward.

449

450 **3 The Source of the High Temperature Anatolian Upper Mantle**

451 3.1 Potential Lower Mantle Roots

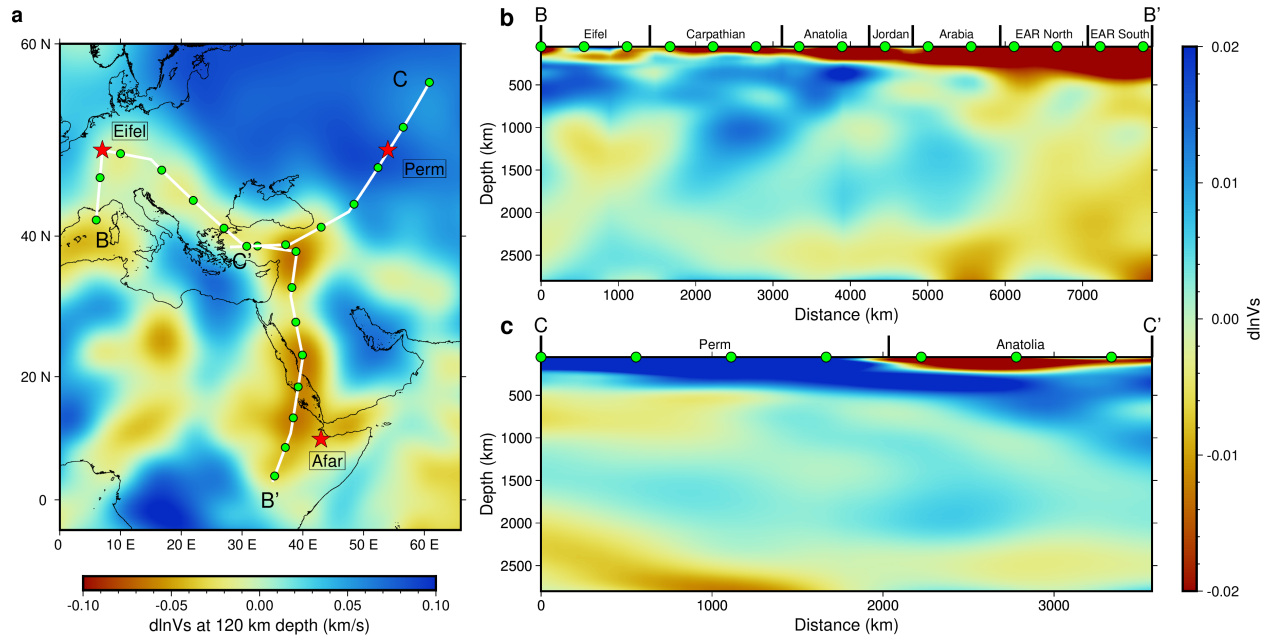
452 To test the idea that the elevated T_P beneath Karacadag reflects high temperature mantle that flows
453 into the upper mantle beneath Anatolia, we searched for the signatures of potential heat sources in
454 multiple global and regional mantle seismic velocity models (Figure 7, S4 & S5), including

455 SEMUCB_WM1 (French & Romanowicz, 2015), GLAD_M25 (Lei et al., 2020),
456 S362WMANI+M (Moulik & Ekström, 2014), EAV09 (Chang et al., 2010), CAM2016 (Ho et al.,
457 2016), 3D2018_08Sv (Debayle et al., 2016), Africa.ANT.Emry-etal.2018 (Emry et al., 2019) and
458 CESM_Europe (Fichtner et al., 2018). Based on these models, no low velocity mantle plume
459 structure coming from the lower mantle is evident beneath Anatolia, and the closest low velocity
460 anomalies that connect to the lower mantle include plume structures beneath the East African Rift
461 system (Afar hotspot) and the Eifel hotspot, as well as the lower mantle Perm Anomaly (Figure 7
462 & S5) (French & Romanowicz, 2015; Lei et al., 2020). However, all of these regions are more
463 than 2000 km away from Anatolia. Although the Perm Anomaly is the closest low velocity lower
464 mantle body, no obvious low velocity anomaly connects it to the Anatolian upper mantle (Figure
465 7c & S5b). In contrast, the EAR region, which lies above a broad plume of low velocity mantle
466 extending from the core-mantle boundary to the upper mantle, is connected to Anatolia through a
467 pronounced channel of low velocity upper mantle (Figure 7, S4 & S5). While a low velocity upper
468 mantle anomaly also connects the Eifel region to Anatolia (Figure 7b and S5a), this anomaly is
469 weaker and shallower than the EAR-Anatolia channel, and the Eifel region is less obviously
470 connected to a deeply-rooted mantle plume. We therefore focus on the mantle plume beneath the
471 EAR as a potential source for the high temperature mantle beneath Anatolia, although we also
472 evaluate the Eifel region.

473 We also acknowledge that other models are possible, for example that a plume connected to the
474 lower mantle actually exists directly beneath Anatolia but has not been imaged, or that some
475 fortuitous combination of regional scale processes (such as extension or delamination in the upper
476 plate lithosphere, or slab roll-back and break-off (Delph et al., 2017; Göğüş & Pysklywec, 2008;
477 Keskin, 2007; Lynner et al.; Memiş et al., 2020)), has contributed to the high Anatolia Tp.

478 However, our focus is to assess whether lateral flow of high temperature asthenosphere over
 479 thousands of kilometers from the EAR is plausible, rather than disproving other scenarios.

480



481

482 **Figure 7.** Shear velocity structure between Anatolia and potential lower mantle roots based on
 483 SEMUCB_WM1 (French & Romanowicz, 2015). (a) Shear velocity perturbation at 120 km depth.
 484 Red stars show surface projections of low-velocity anomalies related to the Afar and Eifel hotspots
 485 (Courtillot et al., 2003) and the lower mantle Perm anomaly (Lekic et al., 2012). Locations of
 486 cross-sections shown in (b) and (c) are indicated by white lines with green markers. The color
 487 scale is shown at the bottom of the panel. (b) and (c) are mantle V_s perturbation cross-sections for
 488 B-B' and C-C' in (a). Geochemical sample geographic group ranges and the surface projections
 489 of the Eifel hotspot and Perm anomaly are labelled at the top. Green symbols correspond to the
 490 same symbols in (a). The color scale for (b) and (c) is on the right side.

491

492 Prior studies have supported the idea that asthenosphere mantle flows from the EAR to Anatolia
 493 based on geochemical data (Ershov & Nikishin, 2004; Faccenna et al., 2013), anisotropy in seismic
 494 wave velocities (Faccenna et al., 2013; Wei et al., 2019), and geodynamical modeling in which
 495 driving forces from plume upwelling and pull from Mediterranean slabs draw upper mantle from

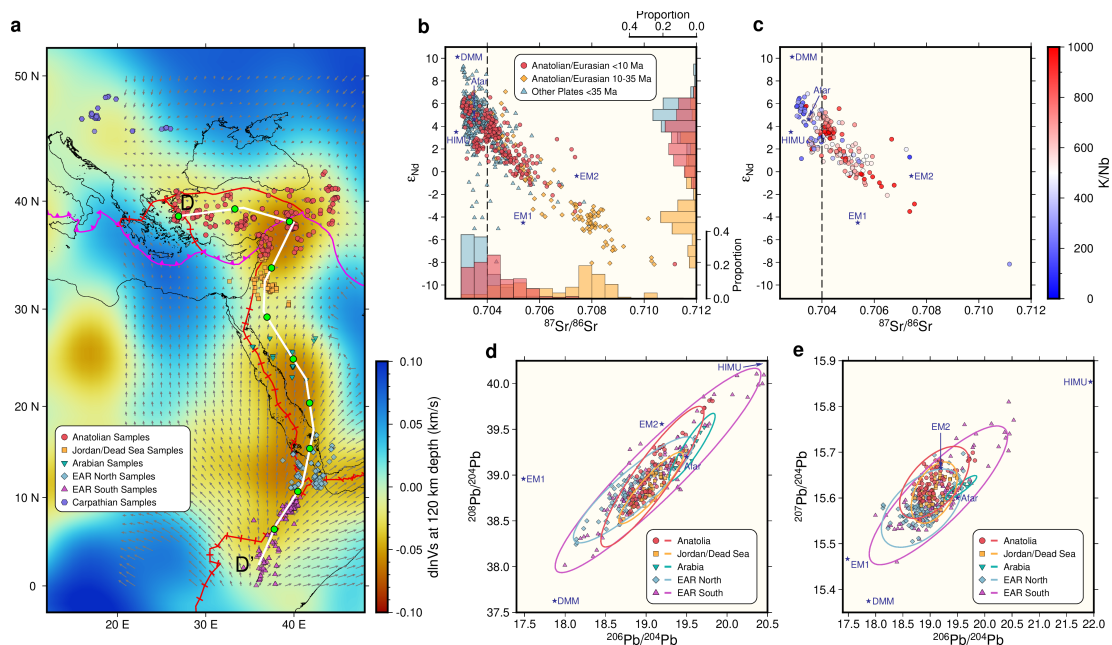
496 the EAR to Anatolia (Faccenna et al., 2013). In addition, this type of flow is also evident in global
 497 mantle flow models (e.g. Conrad & Behn, 2010). In this study, we test the possibility of upper
 498 mantle transport from the EAR to Anatolia using isotopic data and T_P estimates for basalts erupted
 499 along the low velocity channel.

500

501 3.2 Radiogenic Isotope Ratios

502 Radiogenic isotope ratios from 1,004 samples were used to assess whether basalts erupted along
 503 the proposed EAR-Anatolia transport channel share a common mantle isotopic composition
 504 (Figure 8, S6 & S7). The ratios were obtained from the GEOROC database from all studies
 505 including regions from the EAR to Anatolia published between 1990 and 2020. Maximum and
 506 minimum ages for the samples were obtained from their original publications (Supporting
 507 Information Data Set S2).

508



509

510 **Figure 8.** Common isotopic signatures for Anatolian and EAR mantles. (a) V_s perturbations at
511 120 km depth (French & Romanowicz, 2015) show a channel of low velocity mantle that connects
512 the EAR region to Anatolia. Locations of all samples used by Figure 8 & 9 are shown by symbols
513 colored by geographic group. Plate boundaries (Bird, 2003) related to the group division in (b) are
514 in pink (Anatolian/Arabian, Anatolian/African, Eurasian/Arabian and Eurasian/African) and
515 others in red. Subduction boundaries are marked with triangles and divergent boundaries with bars.
516 The white line indicates profile D-D' in Figure 10. Grey arrows show negative horizontal pressure
517 gradients based on the stress field from a global mantle flow model (Conrad & Behn, 2010). (b)
518 $^{87}\text{Sr}/^{86}\text{Sr}$ vs. ϵ_{Nd} from samples grouped by age and tectonic plate (locations in Figure S6a).
519 Histograms show distribution of points in each group. (c) $^{87}\text{Sr}/^{86}\text{Sr}$ vs. ϵ_{Nd} for the Anatolian plate
520 samples < 10Ma in (b), color coded by the K/Nb. (d) $^{206}\text{Pb}/^{204}\text{Pb}$ vs. $^{208}\text{Pb}/^{204}\text{Pb}$ from different
521 geographic groups; ellipses show 95% confidence (locations in Figure S6c). (e) Similar to (d) but
522 for $^{206}\text{Pb}/^{204}\text{Pb}$ vs. $^{207}\text{Pb}/^{204}\text{Pb}$ from different geographic groups (locations in Figure S6d). Stars in
523 (b)-(e) are mantle endmembers (Hofmann, 2007), and the Afar plume composition (Rooney et al.,
524 2012).

525
526 We first analyzed $^{143}\text{Nd}/^{144}\text{Nd}$ and $^{87}\text{Sr}/^{86}\text{Sr}$ isotopes. For this analysis, $^{143}\text{Nd}/^{144}\text{Nd}$ is represented
527 by its relative deviation ϵ_{Nd} which was calculated based on the present-day chondritic value of
528 0.512638 (Hofmann, 2007), and only mafic samples with maximum ages within 35 Ma were used.
529 Values of ϵ_{Nd} versus $^{87}\text{Sr}/^{86}\text{Sr}$ for all samples from the Arabian plate to the EAR for ages less than
530 35 Ma are clustered closely (Figure 8b), consistent with a common source that overlaps suggested
531 values for the Afar plume (Rooney et al., 2012). However, samples from Anatolia on the
532 Eurasian/Anatolian plate (Bird, 2003) show age-dependent results consistent with the region's
533 tectonic evolution (Figure 8b & S6a). Anatolian samples with minimum ages older than 10 Ma,
534 when the Anatolian plate was separated from the Arabian plate by a subducting slab (Cosentino et
535 al., 2011), show high $^{87}\text{Sr}/^{86}\text{Sr}$ and negative ϵ_{Nd} (Figure 8b), consistent with a large contribution
536 from continental sediments that were potentially related to prior subduction (White, 2020). In
537 contrast, Anatolian samples with maximum ages younger than 10 Ma show isotopic ratios that are
538 similar to other regions along the EAR-Anatolia channel, consistent with EAR-sourced mantle
539 entering the asthenosphere beneath Anatolia following the Arabia-Anatolia collision and slab
540 break-off (Cosentino et al., 2011; Faccenna et al., 2013; Wei et al., 2019) (Figure 8b). A similar

541 shift in isotope ratios was also reported in McNab et al. (2018). Some Anatolian samples with ages
542 less than 10 Ma still show $^{87}\text{Sr}/^{86}\text{Sr}$ values higher than 0.704, but similar to what was documented
543 in McNab et al. (2018), most of these samples also show high K/Nb ratios (Figure 8c), which
544 suggests that part of the Anatolian mantle could also be influenced by subduction-modified or
545 lithospheric sources (Class et al., 1998; Gazel et al., 2012a) involved in post-collision processes
546 like lithospheric delamination (Keskin, 2007).

547 We also analyzed Pb isotopes for samples that are not strongly influenced by lithospheric sources
548 to verify mantle source similarity along the EAR-Anatolia channel (Figure 8d & 8e). For the Pb
549 isotope analyses, in addition to the SiO_2 filter, we also required $^{87}\text{Sr}/^{86}\text{Sr}$ to be between 0.7028 and
550 0.7040 to make sure the source compositions based on $^{87}\text{Sr}/^{86}\text{Sr}$ were similar and crustal and sea
551 water influences were eliminated (White, 2020). We also calculated the 95% confidence ellipse
552 for Pb isotope distributions ($^{206}\text{Pb}/^{204}\text{Pb}$, $^{207}\text{Pb}/^{204}\text{Pb}$ & $^{208}\text{Pb}/^{204}\text{Pb}$, Figure 8d & 8e), assuming a
553 normal distribution for all Pb isotope ratios in each geographic group. To avoid outliers in the Pb
554 isotope analyses, samples outside of the 99.9% confidence ellipse were removed; this operation
555 was conducted iteratively until all samples were within the 99.9% confidence ellipse. In what
556 follows, we limited our analysis of samples south of the boundaries between the Anatolian/Arabian
557 plates, Eurasian/Arabian plates and Anatolian/African plates (pink lines in Figure 8a) (Bird, 2003)
558 to those with maximum ages of less than 35 Ma, and limited our analysis of samples north of the
559 boundaries to those with maximum ages less than 10 Ma. Samples along the channel between the
560 EAR and Anatolia were divided into five geographical groups (Figure 8a & S6): the EAR South
561 group contains samples within 0° to 10°N and 30° to 45°E ; the EAR North group contains samples
562 within 10° to 20°N and 38° to 45°E ; the Arabian group contains samples within 20° to 30°N and

563 35° to 45°E; the Jordan/Dead Sea group contains samples within 30° to 35°N and 30° to 45°E; and
564 the Anatolian group contains samples within 35° to 43°N and 30° to 45°E;

565 Based on the filtered samples, both the Anatolian group and the Jordan/Dead Sea group have Pb
566 isotope ratios similar to those observed in the EAR system (Figure 8d & 8e), similar to what was
567 found in Faccenna et al. (2013). A few Arabian samples have slightly more radiogenic $^{206}\text{Pb}/^{204}\text{Pb}$,
568 but the values are still within the 95% confidence range of samples from the southern EAR, while
569 overlapping the Anatolian 95% confidence range. Therefore, the similarity of Sr, Nd and Pb
570 isotopes from different locations along the transport channel, the data from Anatolia since 10 Ma,
571 and the shift in isotope ratios in Anatolia at the 10 Ma Eurasia-Arabia collision (when mantle from
572 the EAR region could more easily reach Anatolia), are all consistent with the hypothesis that
573 asthenospheric mantle beneath Anatolia is derived from a low velocity channel originating from
574 the EAR upper mantle.

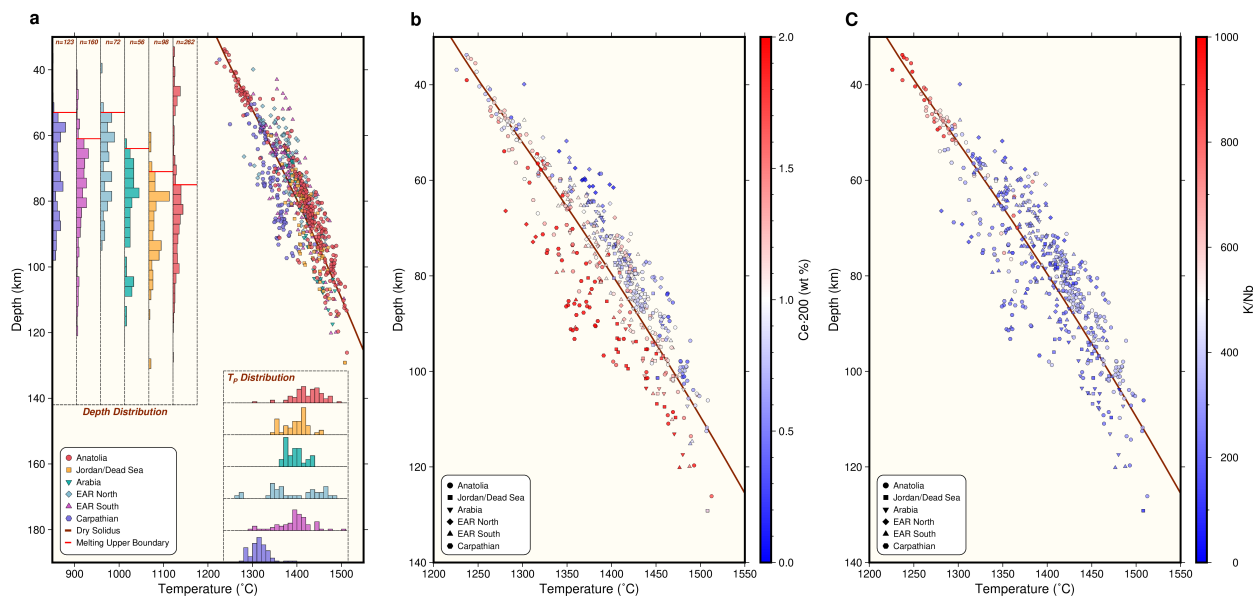
575

576 **4 Thermal Evolution During Asthenospheric Transport**

577 If the plume rising beneath the EAR region is the main heat source for material flowing towards
578 Anatolia, T_P values should not increase along the proposed path of upper mantle transport from
579 the EAR towards Anatolia. To estimate T_P , basaltic primary magma equilibration P-T conditions
580 for 771 volcanic rock samples with major element abundance measurements from the GEOROC
581 database (Supporting Information Data Set S1) along the channel (Figure S6f) were calculated
582 (Lee et al., 2009) with the same method and parameters that were used for the Karacadag samples
583 (Figure 9a). The samples were divided into the same geographic groups that were used for the
584 isotopes applying the same age requirements. The culling operation based on major element

585 composition that was used for Karacadag samples for the T_P modeling was also applied to these
 586 samples, and we assumed the same magma water content (1 wt. %) and oxygen fugacity
 587 ($\text{Fe}^{3+}/\text{Fe}^{\text{Total}} = 0.16$). Since the assumed water content in the melt influences the inferred T_P (e.g.
 588 Figure 4a), to justify the 1 wt. % assumption, the Ce abundances of the samples along the channel
 589 were analyzed (Figure 9b). These values demonstrate that 1 wt. % is a good estimate of water
 590 content. 1 wt. % also agrees with the water abundance from olivine hosted melt inclusions from
 591 samples in Ethiopia and Eritrea (Donovan et al., 2018; Field et al., 2012; Iddon & Edmonds, 2020).

592



593

594 **Figure 9.** Primary magma equilibration along the channel. (a) Primary magma equilibration
 595 conditions from different geographic groups (dots). T_P distribution for each group shown in lower
 596 right histograms, and equilibration depth distribution shown in the upper left histograms, using the
 597 same axes as the main plot. Red bars are the upper limit of melting defined from the equilibration
 598 depth distribution. Red line is the dry solidus (Hirschmann et al., 2009). (b) Primary magma
 599 equilibration conditions color coded by 200 times Ce for basaltic magma samples as a proxy for
 600 the water content. (c) Similar to (b), but color coded by sample K/Nb.

601

602 To ensure that melt equilibration P-T values represent the asthenosphere, we estimated LAB
603 depths for each geographic group by analyzing the distribution of melt equilibration depths (Figure
604 9a), and defining the LAB as the depth where the number of samples in the 10 km beneath it most
605 outnumbers the number of samples in the 10 km above it (similar to what we did for the Karacadag
606 samples). Because samples in each group are not from the same volcanic field and LAB depths
607 for different sample locations may differ, to avoid samples from regions with deeper LAB and thus
608 affected strongly by the lithosphere, we only used samples with equilibration depths more than 15
609 km below the estimated overall LAB depth for each group to estimate mantle T_P (Figure 9a).

610 Equilibration P-T conditions were again assumed to represent the geotherm, and for samples at
611 depths that are not strongly affected by lithospheric conduction, the corresponding adiabatic
612 geotherms and T_P values were estimated through a grid search of mantle adiabats with T_P from
613 1300°C to 1550°C with an interval of 5°C, following the approach in section 2.3 (Figure 9a, lower
614 inset). Samples from the two EAR groups, the Arabian Peninsula and the Jordan/Dead Sea region
615 produced distributions of T_P values that overlap the T_P values from Anatolia (Figure 9a). Some
616 samples from the Anatolian group are clustered at shallower depths, but as noticed before (McNab
617 et al., 2018), these central Anatolian samples share a high K/Nb value, indicating the potential
618 influence of a different geodynamic process that involves water (Figure 9c). The observed elevated
619 mantle T_P over ambient mantle values in these regions is also consistent with the low sodium found
620 in basalts erupted at the Red Sea mid-ocean ridge (Gale et al., 2014). However, although we tried
621 to add basalt samples from the Red Sea to our primary magma analyses, none of them passed the
622 compositional filter. The distribution of T_P values from Anatolia has more samples at slightly
623 higher values than the other regions (Figure 9a), but given potential uncertainties in water content,
624 these minor temperature differences are not significant. We also tested the effect of only including

625 the 394 samples with normalized MgO higher than 9 wt. % (Figure S8) instead of 8 wt. % (Figure
626 9a), but the main conclusions about T_P do not change.

627 The relatively constant T_P values among the different geographic groups along the potential
628 channel are consistent with upper mantle flow from the EAR to Anatolia. However, they also
629 require that only a limited amount of conductive cooling occurs within the channel during the
630 transport, despite the ~2000-3000 km distance.

631 To test whether or not Eifel could be the heat source for the Anatolian mantle, we also analyzed
632 samples from the Carpathian region within 42° to 50°N and 14° to 30°E. If upper mantle was
633 flowing from the Eifel region to Anatolia, along the weaker low velocity channel that connects
634 these zones, it would pass through Carpathian-Pannonian volcanic fields (Figure 7a & S6).
635 Although recent Carpathian samples show isotopic signatures similar to Anatolian samples (Figure
636 S7), consistent with the same mantle source, their T_P values are significantly lower than the basalts
637 erupted on the EAR-Anatolia channel (Figure 9a). This result argues against flow from the Eifel
638 region to Anatolia, because the mantle T_P trend would require an additional heat source en route.
639 If flow from the EAR to Anatolia continues on to the Carpathians, the lower Carpathian T_P would
640 suggest that the effects of cooling become more obvious at these longer transport distances.

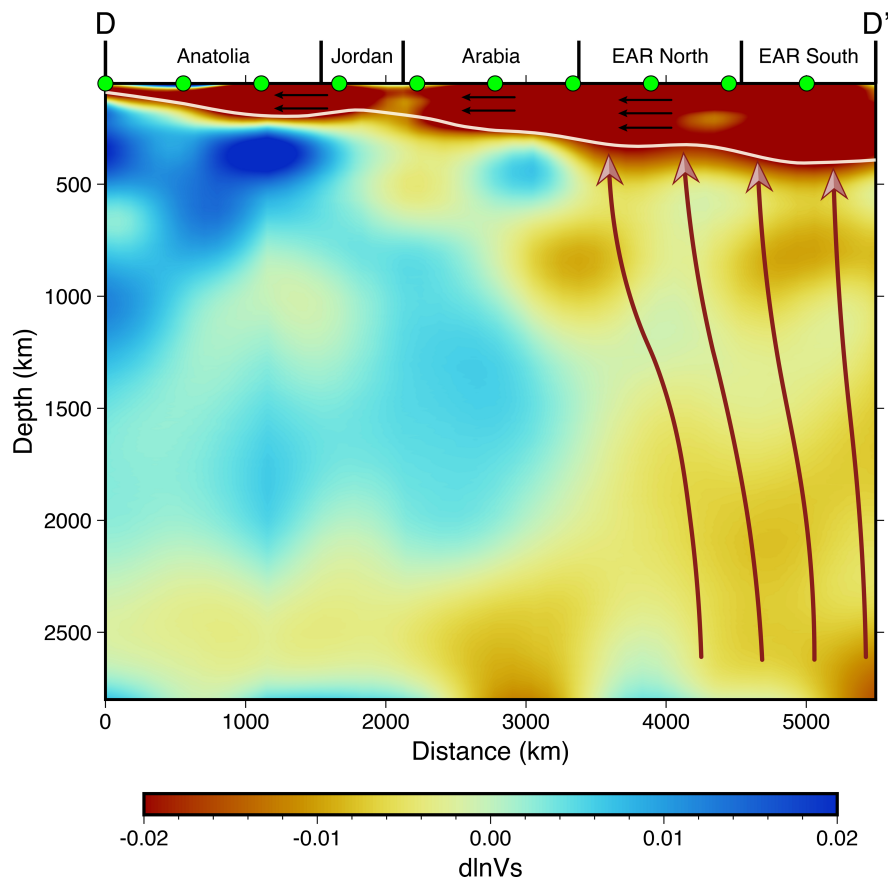
641

642 **5 A Potential Mechanism for the Long-distance Transport**

643 As has been demonstrated in the previous sections, data from different regions along the
644 potential transport channel from the EAR to Anatolia are consistent with a shared mantle source
645 and similar mantle temperatures. These observations can be explained if asthenospheric material

646 can flow laterally over 2000 km distance without much cooling. In this model, as shown in
 647 Figure 10, hot mantle materials would rise upwards within the mantle plume beneath the EAR
 648 system, but after reaching the upper mantle, this hot material would flow towards Anatolia
 649 creating a low seismic velocity channel (Figure 8a) that lies beneath the Red Sea, the western
 650 edge of the Arabian Peninsula, and the eastern edge of the Mediterranean Sea, then finally
 651 reaching Anatolia.

652



653

654 **Figure 10.** Mantle transport from Africa to Anatolia. V_S perturbation (French & Romanowicz,
 655 2015) is shown for cross-section D-D' (Figure 8a). Red arrows show potential paths of deep
 656 mantle upwelling. Black arrows show transport in the asthenosphere through the low velocity
 657 channel from the EAR region to Anatolia. White line shows the estimated maximum channel
 658 depth corresponding to a $d\ln V_S$ of -0.02. At the top, green symbols match the positions of similar
 659 symbols on the map in Figure 8a, and black bars are boundaries of geographic groups.

660

661 The preservation of high mantle temperatures during transport along this asthenospheric channel
662 from the EAR to Anatolia may seem surprising. Since northward plate motion along the channel
663 since 20 Ma is only 2-5 cm/yr (Seton et al., 2012), the asthenosphere driven by plate motions
664 would move slowly enough that it would likely have lost significant heat before reaching
665 Anatolia. However, flow driven by lateral pressure gradients acting on the low-viscosity
666 asthenosphere in the channel due to buoyancy forces provides an alternative mechanism.

667 Here, we develop a 1D model of northward pressure-driven asthenospheric flow to test whether
668 flow rates can be high enough to explain the relatively constant T_P values from the EAR to
669 Anatolia. The presence and geometry of a low viscosity asthenospheric channel are inferred from
670 the seismic velocity profiles shown in Figures 8 & 10, and we assume that the channel has
671 already been completely developed, as supported by various seismic tomography models (Figure
672 7a & S4), and that flow is in steady-state.

673

674 5.1 Pressure Gradients Between the EAR and Anatolia

675 Pressure-driven flow in the direction from the EAR to Anatolia could be viewed in two ways.
676 From the global mantle convection perspective, whole mantle buoyant flows that originate from
677 large-scale density variations (over the whole depth of the mantle) could result in a horizontal
678 pressure gradient within the asthenosphere. For the region of this study, buoyancy forces driving
679 the upwelling mantle plume beneath the EAR would produce a horizontal pressure gradient that
680 pushes hot, low-viscosity material towards Anatolia. Such a northward gradient has been

681 demonstrated in global flow models (Conrad & Behn, 2010; Natarov & Conrad, 2012) (e.g.
682 Figure 8a).

683 From a regional observational perspective, a horizontal asthenospheric pressure gradient could be
684 caused by variations in the thickness of hot asthenospheric material and surface uplift to maintain
685 overall isostatic balance. As plume material upwells beneath the EAR system, it generates uplift,
686 i.e. the observed residual topography high (Yang & Yang, 2021). This upwelling and uplift would
687 produce an excess in upper mantle pressure which pushes hot mantle materials away from the
688 surface expression of the plume (e.g. Bercovici & Lin, 1996; Olson, 1990). The thickness of the
689 buoyant plume-derived asthenosphere would decrease in the direction of mantle flow, as
690 corroborated by seismic velocity structure (French & Romanowicz, 2015) (Figure 10). The
691 northward gradient in the thickness of the channel and its accompanying surface topography would
692 produce a northward pressure gradient. Hence, by evaluating the thickness variation of hot
693 asthenospheric materials from EAR to Anatolia, we could obtain the pressure gradient caused by
694 the thinning of this low-viscosity, low-density asthenospheric layer.

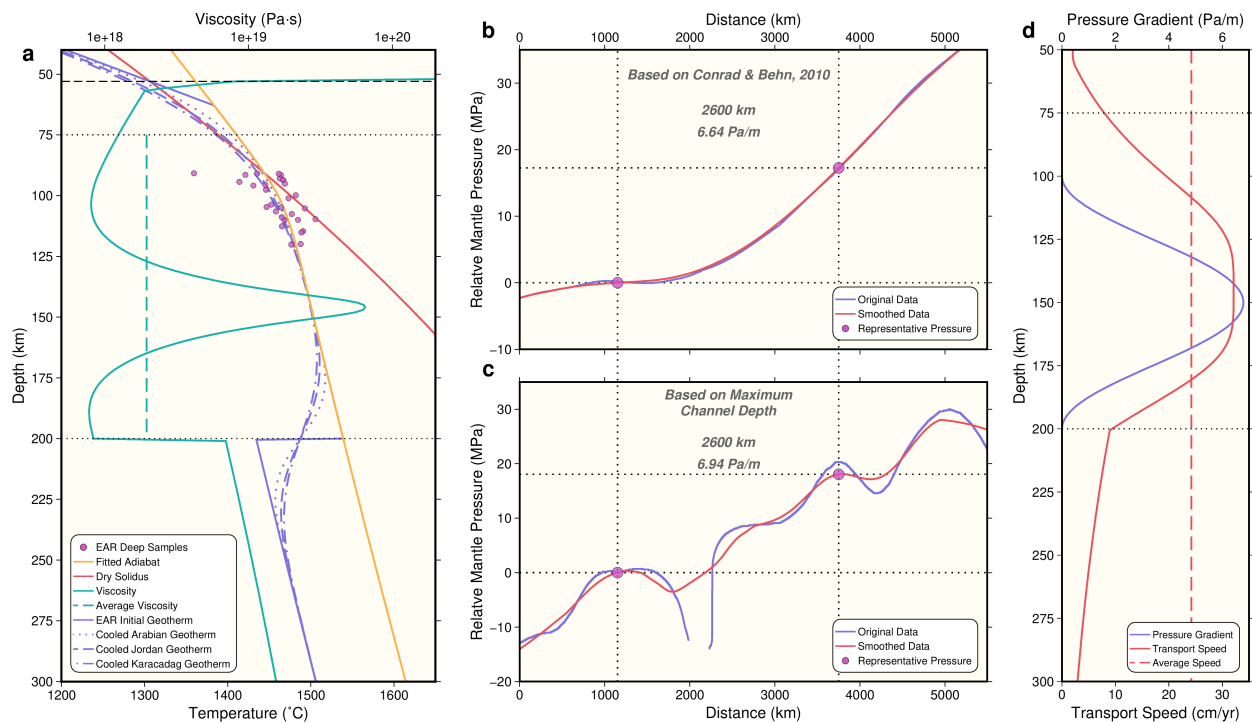
695 In the simple model of Olson (1990), mantle flow at the top of the plume could spread to form a
696 disk of asthenosphere. Alternatively radial outflow at the top of the mantle plume could be
697 concentrated in relatively narrow fingers due to the Saffman-Taylor instability (Schoonman et al.,
698 2017), instead of distributed uniformly and radially in all directions. Fingering could occur because
699 the upwelling mantle would have a much lower viscosity than the ambient mantle due to its higher
700 temperature. For example, as shown in Figure 7a, while the seismic velocities suggest that hot
701 upper mantle materials are concentrated along the channel from the EAR to Anatolia, the hot
702 mantle is also evident along the Gulf of Aden, and a potential finger extends westward as well.
703 Hot material from the plume could thus flow in other than a purely northward direction with a

704 geometry that is even time-dependent. However, our goal in the following discussion is to simply
705 estimate the northward component of flow speed by balancing viscous shear stresses on horizontal
706 planes with the northerly pressure gradient described below. Therefore, the exact geometry of low
707 viscosity fingers and potential east-west horizontal inflows and outflows from/to the channel will
708 not affect the following interpretation, and we are able to ignore flow perpendicular to the channel
709 and treat the flow as 1D to the north. To further validate the 1D flow assumption, we also checked
710 asthenospheric pressure gradients from the global mantle flow model of Conrad and Behn (2010),
711 which also indicates a consistent northward pressure-driven flow in region of the EAR-Anatolia
712 channel (Figure 8a).

713 Asthenospheric pressure gradients and resulting flow velocities between the EAR and Anatolia
714 based on either the large-scale buoyant flow or regional asthenosphere thickness variations were
715 estimated from both global flow models and the observed regional asthenosphere thickness
716 variation. To quantify the horizontal pressure gradient from global buoyant flow, we took the
717 pressure field at 150 km depth from the stress tensors in Conrad and Behn (2010) (Figure 11b; this
718 global mantle flow model includes plate-driven flow, lithosphere net-rotation-driven flow, and
719 buoyant flow driven by density anomalies beneath 325 km depth. To be consistent with the
720 following analyses, these pressure values were smoothed by taking the average of all locations
721 within ± 556 km of the path (Figure 11b), but the smoothed profile is nearly identical to the original
722 one. The pressure gradient was estimated as the pressure difference between the starting point at
723 3750 km (the north edge of the EAR region) and the ending point at 1150 km (near Karacadag) on
724 D-D' (~ 17.3 MPa) divided by the total distance of 2600 km, resulting in a pressure gradient of
725 6.64 Pa/m (Figure 11b). We chose this starting point since it is north of the upwelling plume
726 (Figure 8a & 10), allowing us to ignore vertical flow and focus only on the northward flow in

727 following analyses. Instead of using the great circle distance, we chose to use the path distance on
 728 the D-D' profile that passes through the various volcanic fields. This choice makes the estimates
 729 of possible mantle flow velocities more conservative since a higher pressure gradient would be
 730 obtained if the great circle path was used.

731



732

733 **Figure 11.** Thermal evolution during mantle transport from the EAR to Anatolia. (a) The initial
 734 geotherm at the EAR before transport (solid blue line); cooled geotherms after transport to Arabia
 735 for ~4 Myr (blue dotted line); cooled geotherms after transport to Jordan for ~8 Myr (blue dashed
 736 line); and cooled geotherms after transport to Anatolia for ~10.74 Myr (blue dotted-dashed line).
 737 The initial geotherm is constructed from the EAR adiabat (yellow line) estimated from deep EAR
 738 primary magma equilibration conditions (dots). The red solid line shows the dry solidus. The black
 739 dashed line shows the LAB depth defined by the north EAR samples (upper melting limit; Figure
 740 9a). The equivalent viscosity profile for the initial geotherm is shown by the green solid line with
 741 its scale labeled at the top of the panel, and its averaged log-scale value between the depths of two
 742 black dotted lines is shown by the green dashed line. (b) Relative pressure gradient with respect to
 743 the transport end point in Anatolia at 1150 km (left dotted line) from Conrad and Behn (2010).
 744 The original value is shown by the blue line, and the smoothed gradient averaged over length-
 745 scales of ± 556 km is shown by the red line. The representative pressure drop (magenta dots)
 746 obtained from the starting point in the EAR at 3750 km (right dotted line) and the end point. The
 747 transport length and estimated values for pressure gradient are labelled in gray. (c) Similar to (b)
 748 but for the pressure gradient estimate based on the maximum channel depth. (d) The estimated

749 transport flow speed based on the stress-dependent rheology (red solid line) and its average value
750 between 75 and 200 km depths (red dashed line) with the scale at the bottom. The pressure gradient
751 profile (blue line) with the scale at the top.

752

753 To quantify the pressure gradient based on variations in the asthenospheric channel thickness, we
754 estimated the bottom depth of the potential transport channel as defined by the shear wave velocity
755 structure (Figure 11c). After the upwelling plume impinges on the surface, horizontal mantle flow
756 would form a disk of high-temperature mantle which thins radially (Olson, 1990). Horizontal flow
757 within this layer reflects the balance between the horizontal pressure and the vertical gradient in
758 viscous shear stresses on horizontal planes. If the horizontal mantle flow is concentrated within
759 this disk and not beneath it, vertical buoyancy forces are balanced by surface topography, resulting
760 in a radially uniform pressure and isostasy beneath the disk. Therefore, since pressure is
761 approximately uniform beneath the channel, and the hot plume-affected material has a lower
762 density than the ambient mantle, the slope of the lower boundary of the channel (dz_b / dx) can be
763 translated into a pressure gradient as $\Delta\rho g \cdot dz_b / dx$ (Olson, 1990) within the channel, where $\Delta\rho$
764 is the density difference between hot plume material and ambient mantle, and g is gravitational
765 acceleration. We defined the bottom of the channel on profile B-B' as the depth where $d\ln V_S$
766 (Figure 10) equals -0.02, and smoothed these values within ± 556 km (white line in Figure 10). We
767 chose the value of -0.02 because it defines the lower boundary of the channel just above where
768 $d\ln V_S$ is zero (Figure 10). This choice captures depths where little to no partial melt exists, avoids
769 depths where temperatures are much higher than the solidus and $d\ln V_S$ may be significantly
770 affected by variations in melt fraction, and more accurately reflects where mantle temperature
771 exceeds ambient conditions. In addition, since the estimated pressure gradient depends primarily
772 on the slope of the lower boundary, the absolute $d\ln V_S$ value chosen to represent the boundary

773 does not actually have a significant impact. We assumed that the temperature difference across
774 the channel boundary is 100°C, which is reasonable for mantle material rising from the lower
775 mantle (e.g. Bao et al., 2022), and conservative relative to potential temperature changes associated
776 with a $d\ln V_S$ value of -0.02 (Lee, 2003). With the same solid thermal expansion coefficient that
777 was used for calculating mantle adiabats (Katz et al., 2003) and a reference mantle density of
778 $3.4 \times 10^3 \text{ kg/m}^3$, the corresponding density difference across the channel boundaries $\Delta\rho$ would be
779 13.6 kg/m^3 , which translates into a pressure gradient of 6.94 Pa/m (Figure 11c). This value is
780 similar to the pressure gradient calculated from the large-scale buoyant flow (6.64 Pa/m).

781 Although estimated differently, the pressure gradients from large-scale buoyant flow and
782 asthenospheric channel thickness variation could play a similar role in pushing upwelled material
783 away from the plume. For the global model of Conrad and Behn (2010), a rigid boundary condition
784 is imposed at the surface, which provides the required horizontal mantle pressure gradients for the
785 channel flow. However, if a more realistic traction-free boundary condition is assumed at the
786 surface, and both lithospheric uplift and the asthenospheric channel are included, then instead of
787 the rigid boundary condition, the variations in topography and channel thickness would provide
788 the pressure gradients. Hence, these two estimates of pressure gradients could act similarly to drive
789 horizontal asthenospheric flow. However, because density variations at the depths of the channel
790 are not included in Conrad and Behn (2010), and pressure estimates based on channel thickness
791 do not include dynamic pressures, it would be difficult to judge whether pressure gradients
792 estimated in these two ways are completely equivalent. In any case, we regard these two values as
793 independent pressure gradient estimates, and because their values are similar (0.30 Pa/m
794 difference), we use an intermediate value (6.79 Pa/m) as the reference pressure gradient in the
795 following steps of the 1D flow calculation.

796 Based on the EAR-Anatolia pressure gradient constraints, we constructed a conservative depth
797 profile for the pressure gradient (Figure 11d). In the profile, non-zero pressure only exists between
798 depths of 100 and 200 km, so that the lower boundary is above the base of the channel as defined
799 by the shear-wave velocities in Anatolia (Figure 10). The maximum pressure gradient is the EAR-
800 Anatolia estimate of 6.79 Pa/m, and pressure is represented by a cosine shape function (Figure
801 11d), so the average pressure gradient within the channel is only half of the maximum. This
802 conservative approach is supported by the findings of Natarov and Conrad (2012), who found that
803 the pressure gradient inferred from the asthenospheric infinite strain axis is smaller than the values
804 directly taken from the flow model (Conrad & Behn, 2010). In addition, if the temperature
805 difference between the mantle inside and outside of the channel is less than 100°C, the estimated
806 pressure gradient from the second approach would also be smaller.

807

808 5.2 Thermal Evolution Along the Channel

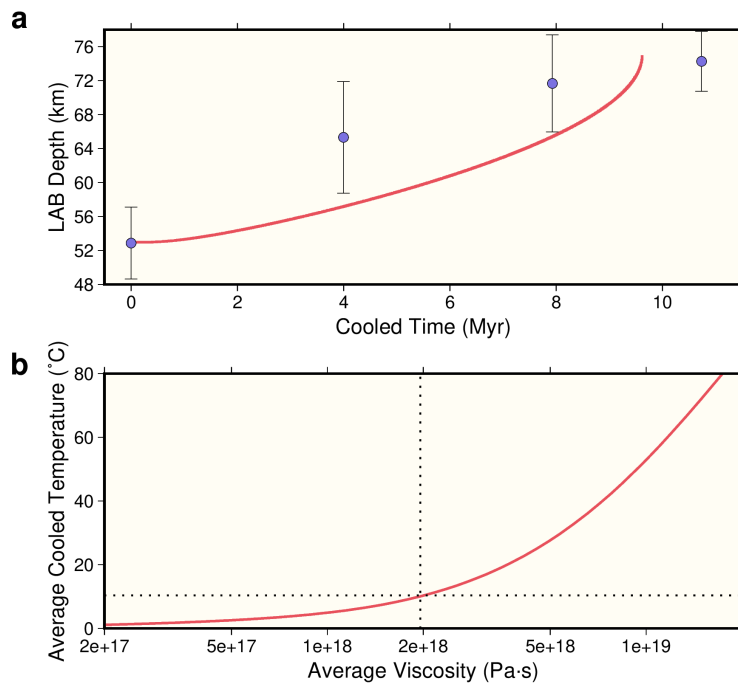
809 The initial EAR mantle geotherm was first estimated based on primary magma equilibration P-T
810 conditions for magma samples from the two EAR groups with equilibration depths below 90 km
811 (Figure 11a). Only these deep samples were employed since these depths are less influenced by
812 the lithosphere and the less well-constrained latent heat of melting. The corresponding EAR
813 adiabat (Figure 11a) was obtained by assuming a mantle water content of 100 wt. ppm (as found
814 in Karacadag) and by searching for the best-fitting mantle T_P with the grid search approach similar
815 to that used in section 2.3 that minimizes $\|T_{sample} - T_{geo}\|_2$. The resulting EAR T_P value is 1408°C.

816 We used a semi-analytical method to solve for the depth distribution of flow speed, assuming a
817 stress-dependent mantle rheology that considers both dislocation and diffusion creep (Hirth &
818 Kohlstedt, 2003) and calibrations of FTIR data in olivine (Bell et al., 2003). The details of the
819 rheology and flow calculations are in Supporting Information Text S4. The resulting
820 asthenospheric flow as a function of depth is shown in Figure 11d. Between the overall LAB depth
821 from Anatolian basalt samples (75 km, Figure 9a) and the lower boundary of the channel in
822 Anatolia (200 km, Figure 10), the average flow speed is 24.2 cm/yr. This rate, while high, is
823 comparable to upper mantle flow rates estimated in the South Pacific (Ballmer et al., 2013), within
824 the range estimated near North Atlantic Ridges (Parnell-Turner et al., 2017), and lower than the
825 estimated rates in another North Atlantic study (Hartley et al., 2011). With a 24.2 cm/yr
826 asthenospheric flow rate, mantle materials would travel the 2600 km distance from the EAR to
827 Anatolia in 10.74 Myr.

828 Given the estimated transport time from the EAR to Anatolia, we modeled thermal evolution
829 within the channel to evaluate whether cooling in the channel is small enough to be consistent with
830 the minimal variation among observed mantle potential temperatures along the transport path. For
831 the initial geotherm at the beginning of the transport in EAR, a conductive geotherm for the
832 lithosphere was used to link the adiabatic temperature in the asthenosphere to 0°C at the surface.
833 We also required that this geotherm crossed the dry solidus at 53 km depth in accordance with the
834 LAB (upper melting limit) inferred from the basalt samples in the northern EAR group (Figure
835 9a). At depths below 200 km, a 100°C temperature decrease from the adiabat defined by the EAR
836 deep samples was imposed so that the mantle beneath the channel is at a typical ambient mantle
837 temperatures (purple line in Figure 11a). Details for how the initial geotherm was parameterized
838 appear in Supporting Information Text S4.

839 To estimate cooling along the transport path, the initial geotherm was allowed to cool over time
 840 intervals corresponding to the transport times to the Arabian volcanic fields (~ 4 Myr), the
 841 Jordan/Dead Sea volcanic fields (~ 8 Myr) and to Anatolia (near Karacadag; 10.74 Myr) (Figure
 842 11a). While the shallower part of the geotherm cools significantly over these time-scales,
 843 temperatures at depths greater than 75 km are largely unchanged, especially for depths over 100
 844 km. Since the mantle T_P values are based on the basalt samples with equilibration depths greater
 845 than 75 km, the cooling models explain how similar mantle T_P values can be observed in the
 846 different regions along the EAR-Anatolia transport channel.

847



848

849 **Figure 12.** Cooling related tests. (a) LAB deepening with cooling. Blue dots show the LAB depth
 850 determined from the distribution of basalt equilibration depths (the upper limit of melting) (Figure
 851 9a) for the north EAR (0 Myr), Arabia (~ 4 Myr), Jordan/Dead Sea (~ 8 Myr) and Anatolia (~ 10.74
 852 Myr). Error bars show twice the standard deviation of the LAB depths. The red line shows the
 853 depth where the upper part of the cooled geotherm crosses the dry solidus (Figure 11a) which
 854 could indicate the upper limit of melting, for different cooling times. (b) The average temperature
 855 at the depths of the Anatolian basalt samples after transport to Anatolia (~ 10.74 Myr of cooling)

856 with respect to the average equivalent viscosity between 75 and 200 km depths. Black dotted lines
857 mark the value for the case in Figure 11.

858

859 To further test the cooling during channel flow model, we compared the LAB depths inferred from
860 the basalts (Figure 9a, upper inset) with LAB depths predicted by the cooling. In the cooling model,
861 as lithospheric conduction and cooling progress, the upper intersection of the geotherm and the
862 dry solidus moves to deeper depths (Figure 11a). The shallowest depth at which primary magmas
863 could equilibrate thus gets deeper as well. This prediction (red line in Figure 12a) is broadly
864 matched by the deepening of the basalt-inferred LAB (Figure 12a) along the channel from the
865 northern EAR to Anatolia. The uncertainty of the basalt-inferred LAB was obtained by
866 bootstrapping the basalt samples in each group that were used for determining that LAB depth
867 (Figure 12a). The overall trends in predicted and observed depths are similar, and given
868 uncertainties in the initial geotherm (which depends strongly on the assumed water content in the
869 melt), local tectonic histories, and calculation of pressures of last equilibration, misfits at specific
870 cooling times can easily be accounted for. The overall match between predicted and observed
871 depths provides support that the cooling model is plausible for transport along the EAR-Anatolia
872 channel.

873 Since actual mantle rheology may differ from the experimentally-constrained rheology assumed
874 in the flow model, we also tested the effect of different viscosity models on flow rates and potential
875 cooling of the asthenosphere along the EAR-Anatolia channel. In the experimentally-constrained
876 case discussed so far, the equivalent viscosity for the stress-dependent rheology is calculated as
877 the shear stress (τ) divided by the strain rate (dv/dz), where v is the horizontal flow speed, and
878 z is depth (solid green line in Figure 11a). The very high equivalent viscosity near 150 km depth
879 is due to the very small strain rate (evident from the flow speed profile in Figure 11d) and the

880 stress-dependent nature of dislocation creep. In the first alternative viscosity model, we instead
881 used the average value of the log-scaled viscosities between 75 and 200 km depths to represent the
882 overall viscosity, which is $\sim 2 \times 10^{18}$ Pa·s (dashed green line in Figure 11a). We also systematically
883 varied the magnitude of viscosity between 75 and 200 km depth by varying the pre-factors of the
884 dislocation and diffusion creep flow laws (Supporting Information Text S4). For each of these
885 new viscosity profiles, we calculated the average viscosity between 75 and 200 km depths and the
886 EAR-Anatolia transport time and the degree of cooling. Cooling was measured by the average
887 temperature decrease at the depths corresponding to Anatolian basalt samples (deeper than 90 km).
888 For the average viscosity of $\sim 2 \times 10^{18}$ Pa·s, the overall cooling is only $\sim 10^\circ\text{C}$ (Figure 12b), and for
889 viscosities less than 5×10^{18} Pa·s, cooling is still small enough to be consistent with the observed
890 T_P distributions. This comparison shows that asthenospheric flow rates fast enough to match the
891 modest cooling evident in the T_P distributions along the transport channel are possible, but only
892 for relatively low asthenospheric viscosities, as would be expected for the elevated T_P values from
893 EAR to Anatolia. In other words, this type of fast asthenospheric transport is plausible in high
894 temperature regions of the mantle, but probably not globally.

895 Compared with published mantle viscosities estimated with different methods, the viscosities
896 assumed in the flow rate calculations at or above 5×10^{17} Pa·s are reasonable. They are higher
897 than the lower bound for asthenospheric viscosity of 5×10^{17} Pa·s constrained by seasonal
898 deformation (Chanard et al., 2018), within the range of the mantle viscosity suggested from
899 postseismic deformation beneath Indian Ocean as $(0.5-10) \times 10^{18}$ Pa·s (Hu et al., 2016), and lower
900 than the upper bound for asthenospheric viscosity of 10^{19} Pa·s estimated from the geoid variation
901 across an ocean basin fracture zone (Craig & McKenzie, 1986). However, we also recognize that

902 the different time-scales of these processes need to be taken into account when making viscosity
903 comparisons (e.g. Lau et al., 2021).

904

905 **6 Conclusions and Implications**

906 In this study, we demonstrated that a wide range of seismic and geochemical observations are
907 consistent with a model in which hot asthenosphere beneath Anatolia is fed by long-distance lateral
908 transport of upper mantle from East Africa, with the lateral flow being driven by pressure gradients
909 created by the buoyancy of the African mantle plume. These conclusions are based on a series of
910 analyses.

911 1. We determined the mantle potential temperature beneath the Karacadag volcanic field in
912 eastern Anatolia to be $\sim 1420^{\circ}\text{C}$, higher than typical of ambient mantle, based on joint modeling
913 of primary magma equilibration pressure-temperature conditions from basalt samples and a
914 seismic velocity gradient imaged by S_p receiver functions that is consistent with the onset of
915 partial melting.

916 2. Tomographic models show that no obvious deep mantle plume exists beneath Anatolia, but
917 they consistently show a channel of low seismic velocity upper mantle that connects Anatolia
918 and the East African Rift, as has been proposed by prior studies (Ershov & Nikishin, 2004;
919 Faccenna et al., 2013; Wei et al., 2019).

920 3. In a chain of magmatic field along the proposed transport path from the East African Rift
921 system to Anatolia, we assessed available radiogenic isotope ratios in basalt samples, including

922 $^{143}\text{Nd}/^{144}\text{Nd}$, $^{87}\text{Sr}/^{86}\text{Sr}$, $^{208}\text{Pb}/^{204}\text{Pb}$, $^{207}\text{Pb}/^{204}\text{Pb}$ and $^{206}\text{Pb}/^{204}\text{Pb}$, and found they are consistent
923 with a shared mantle source.

924 4. To evaluate thermal evolution along the transport channel, we analyzed primary magma
925 equilibration P-T conditions from the basalts, and found that any decreases in mantle potential
926 temperature are minimal, indicating little cooling within the asthenospheric channel.

927 5. To assess whether the observed mantle potential temperatures are physically consistent with
928 flow over thousands of kilometers in the channel, we modelled potential mantle transport time
929 from East Africa to Anatolia for pressure-driven flow, created by the African plume, and a
930 stress-dependent rheology. With conservative assumptions, asthenospheric mantle from East
931 Africa could reach Anatolia in 11 Myr. By modeling conductive cooling of the geotherm for
932 ~11 Myr, we found that while the shallowest asthenosphere is significantly cooled, leading to
933 an increase in the depth of the LAB that is matched by basalt sample constraints, temperature
934 changes in the deeper asthenosphere are small, consistent with the observed elevated mantle
935 potential temperatures all along the channel. In addition to the horizontal pressure gradient
936 provided by the mantle plume, another factor needed to enable this type of rapid asthenospheric
937 flow is a low viscosity, as would be expected for the elevated temperature of plume-affected
938 mantle.

939 The type of rapid pressure-driven asthenospheric flow over length-scales of thousands of
940 kilometers supported by this study (Figure 10) has important implications for heat and material
941 transport in the Earth. The 2000-3000 km length-scale from East Africa to Anatolia exceeds some
942 previously inferred cases of long-distance transport of hot plume materials from their plume roots
943 (Ebinger & Sleep, 1998; Schoonman et al., 2017), and rivals others (Ballmer et al., 2013). Rapid

944 asthenospheric flow from plumes and the preservation of high mantle temperatures that it enables
945 help to explain massive Large Igneous Provinces earlier in Earth history, such as the Central
946 Atlantic Magmatic Province (Marzoli et al., 1999) and in the Pacific (Madrigal et al., 2016; Stern
947 et al., 2020). While the inferred rates of asthenospheric flow from the EAR to Anatolia are higher
948 than regional plate velocities, they are actually comparable to the pressure-driven asthenospheric
949 flow velocities implied by the age-progression of volcanic chains from the Pacific superswell
950 towards the southern East Pacific Rise (Ballmer et al., 2013) and in the North Atlantic (Hartley et
951 al., 2011; Parnell-Turner et al., 2017). Mantle flow driven by plume-related pressure gradients are
952 relevant to understanding the distribution of magmatism on terrestrial planets such as Venus which
953 have plume-like upwellings (Smrekar et al., 2010) in the absence of plate tectonics. Overall, the
954 results of this study indicate that high temperature plume-influenced materials can reach much
955 farther in the upper mantle and over larger volumes of the Earth than commonly assumed.

956

957 **Acknowledgements**

958 We thank E. Bozdog for providing the global adjoint tomography model GLAD_M25, N. Blom
959 and A. Fichtner for the Anatolian velocity models, M. Behn for the Conrad and Behn (2010) flow
960 model, and C. Dalton for assistance with Perple_X and discussion. We thank P. Antoshechkina,
961 Y. Liang and B. Liu for discussions of melting modeling and interpretation. We thank S. Grand
962 for the discussions. This paper was partially supported by the National Science Foundation grant
963 EAR-1829401.

964

965 **Open Research**

966 The Sp receiver function common-conversion point stack is available upon request.
967 Geochemical and petrological data were downloaded from GEOROC ([http://georoc.mpch-](http://georoc.mpch-mainz.gwdg.de/Georoc)
968 [mainz.gwdg.de/Georoc](http://georoc.mpch-mainz.gwdg.de/Georoc)) and are provided in the supporting information. Velocity model
969 SEMUCB_WM1 was downloaded from the Berkeley Global Seismology Group
970 (http://seismo.berkeley.edu/wiki_br/Main_Page). Velocity model GLAD_M25 was obtained
971 from E. Bozdog, the velocity model in (Blom et al., 2020) from N. Blom, and the velocity model
972 in (Fichtner et al., 2013) from A. Fichtner; other velocity models are from the IRIS archive
973 (<https://ds.iris.edu/ds/products/emc-earthmodels/>). All computer codes used for data processing,
974 analysis, and plotting are available upon request. All the figures are generated with the Generic
975 Mapping Tools (Wessel et al., 2019).

976

977 **References**

- 978 Abers, G. A., Fischer, K., Hirth, G., Wiens, D., Plank, T., Holtzman, B. K., et al. (2014).
979 Reconciling mantle attenuation-temperature relationships from seismology, petrology,
980 and laboratory measurements. *Geochemistry, Geophysics, Geosystems*, 15(9), 3521-3542.
981 doi.org/10.1002/2014GC005444
- 982 Ballmer, M. D., Conrad, C. P., Smith, E. I., & Harmon, N. (2013). Non-hotspot volcano chains
983 produced by migration of shear-driven upwelling toward the East Pacific Rise. *Geology*,
984 41(4), 479-482.

- 985 Bao, X., Lithgow-Bertelloni, C. R., Jackson, M. G., & Romanowicz, B. (2022). On the relative
986 temperatures of Earth's volcanic hotspots and mid-ocean ridges. *Science*, 375(6576), 57-
987 61.
- 988 Bell, D. R., Rossman, G. R., Maldener, J., Endisch, D., & Rauch, F. (2003). Hydroxide in
989 olivine: A quantitative determination of the absolute amount and calibration of the IR
990 spectrum. *Journal of Geophysical Research: Solid Earth*, 108(B2).
- 991 Bercovici, D., & Lin, J. (1996). A gravity current model of cooling mantle plume heads with
992 temperature-dependent buoyancy and viscosity. *Journal of Geophysical Research: Solid*
993 *Earth*, 101(B2), 3291-3309.
- 994 Berk Biryol, C., Beck, S. L., Zandt, G., & Özacar, A. A. (2011). Segmented African lithosphere
995 beneath the Anatolian region inferred from teleseismic P-wave tomography. *Geophysical*
996 *Journal International*, 184(3), 1037-1057. 10.1111/j.1365-246X.2010.04910.x
- 997 Bird, P. (2003). An updated digital model of plate boundaries. *Geochemistry, Geophysics,*
998 *Geosystems*, 4(3). doi.org/10.1029/2001GC000252
- 999 Blom, N., Gokhberg, A., & Fichtner, A. (2020). Seismic waveform tomography of the central
1000 and eastern Mediterranean upper mantle. *Solid Earth*, 11(2), 669-690.
- 1001 Chanard, K., Fleitout, L., Calais, E., Barbot, S., & Avouac, J. P. (2018). Constraints on transient
1002 viscoelastic rheology of the asthenosphere from seasonal deformation. *Geophysical*
1003 *Research Letters*, 45(5), 2328-2338.
- 1004 Chang, S. J., Van Der Lee, S., Flanagan, M. P., Bedle, H., Marone, F., Matzel, E. M., et al.
1005 (2010). Joint inversion for three-dimensional S velocity mantle structure along the
1006 Tethyan margin. *Journal of Geophysical Research: Solid Earth*, 115(B8).

- 1007 Cirmik, A. (2018). Examining the crustal structures of eastern Anatolia, using thermal gradient,
1008 heat flow, radiogenic heat production and seismic velocities. *Bollettino di Geofisica*
1009 *Teorica ed Applicata*, 59(2), 117-134.
- 1010 Class, C., Goldstein, S. L., Altherr, R., & Bachèlery, P. (1998). The process of plume–
1011 lithosphere interactions in the ocean basins—the case of Grande Comore. *Journal of*
1012 *Petrology*, 39(5), 881-903.
- 1013 Connolly, J. (2009). The geodynamic equation of state: what and how. *Geochemistry,*
1014 *Geophysics, Geosystems*, 10(10). doi.org/10.1029/2009GC002540
- 1015 Conrad, C. P., & Behn, M. D. (2010). Constraints on lithosphere net rotation and asthenospheric
1016 viscosity from global mantle flow models and seismic anisotropy. *Geochemistry,*
1017 *Geophysics, Geosystems*, 11(5), n/a-n/a. 10.1029/2009gc002970
- 1018 Conrad, C. P., Bianco, T. A., Smith, E. I., & Wessel, P. (2011). Patterns of intraplate volcanism
1019 controlled by asthenospheric shear. *Nature Geoscience*, 4(5), 317-321. 10.1038/ngeo1111
- 1020 Cosentino, D., Schildgen, T. F., Cipollari, P., Faranda, C., Gliozzi, E., Hudackova, N., et al.
1021 (2011). Late Miocene surface uplift of the southern margin of the Central Anatolian
1022 Plateau, Central Taurides, Turkey. *Geological Society of America Bulletin*, 124(1-2),
1023 133-145. 10.1130/b30466.1
- 1024 Courtier, A. M., Jackson, M. G., Lawrence, J. F., Wang, Z., Lee, C.-T. A., Halama, R., et al.
1025 (2007). Correlation of seismic and petrologic thermometers suggests deep thermal
1026 anomalies beneath hotspots. *Earth and Planetary Science Letters*, 264(1-2), 308-316.
- 1027 Courtillot, V., Davaille, A., Besse, J., & Stock, J. (2003). Three distinct types of hotspots in the
1028 Earth's mantle. *Earth and Planetary Science Letters*, 205(3-4), 295-308.

- 1029 Craig, C. H., & McKenzie, D. (1986). The existence of a thin low-viscosity layer beneath the
1030 lithosphere. *Earth and Planetary Science Letters*, 78(4), 420-426.
- 1031 Dalton, C. A., Langmuir, C. H., & Gale, A. (2014). Geophysical and geochemical evidence for
1032 deep temperature variations beneath mid-ocean ridges. *Science*, 344(6179), 80-83.
- 1033 Dasgupta, R., Hirschmann, M. M., & Smith, N. D. (2007). Water follows carbon: CO₂ incites
1034 deep silicate melting and dehydration beneath mid-ocean ridges. *Geology*, 35(2).
1035 10.1130/g22856a.1
- 1036 Debayle, E., Dubuffet, F., & Durand, S. (2016). An automatically updated S-wave model of the
1037 upper mantle and the depth extent of azimuthal anisotropy. *Geophysical Research
1038 Letters*, 43(2), 674-682.
- 1039 Delph, J. R., Abgarmi, B., Ward, K. M., Beck, S. L., Özacar, A. A., Zandt, G., et al. (2017). The
1040 effects of subduction termination on the continental lithosphere: Linking volcanism,
1041 deformation, surface uplift, and slab tearing in central Anatolia. *Geosphere*, 13(6), 1788-
1042 1805.
- 1043 Dixon, J. E., & Clague, D. A. (2001). Volatiles in basaltic glasses from Loihi Seamount, Hawaii:
1044 Evidence for a relatively dry plume component. *Journal of Petrology*, 42(3), 627-654.
- 1045 Dixon, J. E., Leist, L., Langmuir, C., & Schilling, J.-G. (2002). Recycled dehydrated lithosphere
1046 observed in plume-influenced mid-ocean-ridge basalt. *Nature*, 420(6914), 385-389.
- 1047 Donovan, A., Blundy, J., Oppenheimer, C., & Buisman, I. (2018). The 2011 eruption of Nabro
1048 volcano, Eritrea: perspectives on magmatic processes from melt inclusions. *Contributions
1049 to Mineralogy and Petrology*, 173(1), 1-23.
- 1050 Ebinger, C. J., & Sleep, N. (1998). Cenozoic magmatism throughout east Africa resulting from
1051 impact of a single plume. *Nature*, 395(6704), 788-791.

- 1052 Emry, E. L., Shen, Y., Nyblade, A. A., Flinders, A., & Bao, X. (2019). Upper mantle earth
1053 structure in Africa from full-wave ambient noise tomography. *Geochemistry, Geophysics,*
1054 *Geosystems*, 20(1), 120-147. doi.org/10.1029/2018GC007804
- 1055 Ershov, A., & Nikishin, A. (2004). Recent geodynamics of the Caucasus-Arabia-east Africa
1056 region. *Geotectonics*, 38(2), 123-136.
- 1057 Faccenna, C., Becker, T. W., Jolivet, L., & Keskin, M. (2013). Mantle convection in the Middle
1058 East: Reconciling Afar upwelling, Arabia indentation and Aegean trench rollback. *Earth*
1059 *and Planetary Science Letters*, 375, 254-269. 10.1016/j.epsl.2013.05.043
- 1060 Fichtner, A., Saygin, E., Taymaz, T., Cupillard, P., Capdeville, Y., & Trampert, J. (2013). The
1061 deep structure of the North Anatolian Fault Zone. *Earth and Planetary Science Letters*,
1062 373, 109-117. 10.1016/j.epsl.2013.04.027
- 1063 Fichtner, A., van Herwaarden, D. P., Afanasiev, M., Simuté, S., Krischer, L., Çubuk-Sabuncu,
1064 Y., et al. (2018). The collaborative seismic earth model: generation 1. *Geophysical*
1065 *Research Letters*, 45(9), 4007-4016.
- 1066 Field, L., Barnie, T., Blundy, J., Brooker, R. A., Keir, D., Lewi, E., & Saunders, K. (2012).
1067 Integrated field, satellite and petrological observations of the November 2010 eruption of
1068 Erta Ale. *Bulletin of Volcanology*, 74(10), 2251-2271.
- 1069 French, S. W., & Romanowicz, B. (2015). Broad plumes rooted at the base of the Earth's mantle
1070 beneath major hotspots. *Nature*, 525(7567), 95-99.
- 1071 Gale, A., Langmuir, C. H., & Dalton, C. A. (2014). The global systematics of ocean ridge basalts
1072 and their origin. *Journal of Petrology*, 55(6), 1051-1082.
- 1073 Gazel, E., Plank, T., Forsyth, D. W., Bendersky, C., Lee, C.-T. A., & Hauri, E. H. (2012a).
1074 Lithosphere versus asthenosphere mantle sources at the Big Pine Volcanic Field,

- 1075 California. *Geochemistry, Geophysics, Geosystems*, 13(6), n/a-n/a.
- 1076 10.1029/2012gc004060
- 1077 Gazel, E., Plank, T., Forsyth, D. W., Bendersky, C., Lee, C. T. A., & Hauri, E. H. (2012b).
- 1078 Lithosphere versus asthenosphere mantle sources at the Big Pine Volcanic Field,
- 1079 California. *Geochemistry, Geophysics, Geosystems*, 13(6).
- 1080 doi.org/10.1029/2012GC004060
- 1081 Göğüş, O. H., & Pysklywec, R. N. (2008). Mantle lithosphere delamination driving plateau uplift
- 1082 and synconvergent extension in eastern Anatolia. *Geology*, 36(9), 723-726.
- 1083 Grose, C. J., & Afonso, J. C. (2013). Comprehensive plate models for the thermal evolution of
- 1084 oceanic lithosphere. *Geochemistry, Geophysics, Geosystems*, 14(9), 3751-3778.
- 1085 Hansen, S. E., Nyblade, A. A., & Benoit, M. H. (2012). Mantle structure beneath Africa and
- 1086 Arabia from adaptively parameterized P-wave tomography: Implications for the origin of
- 1087 Cenozoic Afro-Arabian tectonism. *Earth and Planetary Science Letters*, 319, 23-34.
- 1088 Hartley, R. A., Roberts, G. G., White, N., & Richardson, C. (2011). Transient convective uplift
- 1089 of an ancient buried landscape. *Nature Geoscience*, 4(8), 562-565.
- 1090 Herzberg, C., & Asimow, P. D. (2008). Petrology of some oceanic island basalts: PRIMELT2.
- 1091 XLS software for primary magma calculation. *Geochemistry, Geophysics, Geosystems*,
- 1092 9(9). doi.org/10.1029/2008GC002057
- 1093 Herzberg, C., Asimow, P. D., Arndt, N., Niu, Y., Leshner, C., Fitton, J., et al. (2007).
- 1094 Temperatures in ambient mantle and plumes: Constraints from basalts, picrites, and
- 1095 komatiites. *Geochemistry, Geophysics, Geosystems*, 8(2).
- 1096 doi.org/10.1029/2006GC001390

- 1097 Herzberg, C., & Gazel, E. (2009). Petrological evidence for secular cooling in mantle plumes.
1098 *Nature*, 458(7238), 619-622.
- 1099 Hirschmann, M. M. (2010). Partial melt in the oceanic low velocity zone. *Physics of the Earth*
1100 *and Planetary Interiors*, 179(1-2), 60-71. 10.1016/j.pepi.2009.12.003
- 1101 Hirschmann, M. M., Tenner, T., Aubaud, C., & Withers, A. C. (2009). Dehydration melting of
1102 nominally anhydrous mantle: The primacy of partitioning. *Physics of the Earth and*
1103 *Planetary Interiors*, 176(1-2), 54-68. 10.1016/j.pepi.2009.04.001
- 1104 Hirth, G., & Kohlstedt, D. L. (2003). Rheology of the upper mantle and the mantle wedge: A
1105 view from the experimentalists. *Geophysical Monograph-American Geophysical Union*,
1106 138, 83-106.
- 1107 Ho, T., Priestley, K., & Debayle, E. (2016). A global horizontal shear velocity model of the
1108 upper mantle from multimode Love wave measurements. *Geophysical Journal*
1109 *International*, 207(1), 542-561.
- 1110 Hofmann, A. W. (2007). Sampling mantle heterogeneity through oceanic basalts: isotopes and
1111 trace elements. In H. D. Holland & K. K. Turekian (Eds.), *Treatise on Geochemistry* (pp.
1112 1-44). Oxford: Pergamon.
- 1113 Hu, Y., Bürgmann, R., Banerjee, P., Feng, L., Hill, E. M., Ito, T., et al. (2016). Asthenosphere
1114 rheology inferred from observations of the 2012 Indian Ocean earthquake. *Nature*,
1115 538(7625), 368-372.
- 1116 Hua, J., Fischer, K. M., Mancinelli, N. J., & Bao, T. (2020). Imaging with pre-stack migration
1117 based on Sp scattering kernels. *Geophysical Journal International*, 220(1), 428-449.

- 1118 Hua, J., Fischer, K. M., & Savage, M. K. (2018). The lithosphere–asthenosphere boundary
1119 beneath the South Island of New Zealand. *Earth and Planetary Science Letters*, 484, 92-
1120 102.
- 1121 Hua, J., Fischer, K. M., Wu, M., & Blom, N. (2020). New Approaches to Multifrequency Sp
1122 Stacking Tested in the Anatolian Region. *Journal of Geophysical Research: Solid Earth*,
1123 125(11). doi.org/10.1029/2020JB020313
- 1124 Iddon, F., & Edmonds, M. (2020). Volatile-rich magmas distributed through the upper crust in
1125 the Main Ethiopian Rift. *Geochemistry, Geophysics, Geosystems*, 21(6),
1126 e2019GC008904.
- 1127 Iwamori, H., McKenzie, D., & Takahashi, E. (1995). Melt generation by isentropic mantle
1128 upwelling. *Earth and Planetary Science Letters*, 134(3-4), 253-266.
- 1129 Jackson, I., & Faul, U. H. (2010). Grainsize-sensitive viscoelastic relaxation in olivine: Towards
1130 a robust laboratory-based model for seismological application. *Physics of the Earth and*
1131 *Planetary Interiors*, 183(1-2), 151-163.
- 1132 Katz, R. F., Spiegelman, M., & Langmuir, C. H. (2003). A new parameterization of hydrous
1133 mantle melting. *Geochemistry, Geophysics, Geosystems*, 4(9), n/a-n/a.
1134 10.1029/2002gc000433
- 1135 Keskin, M. (2007). Eastern Anatolia: A hotspot in a collision zone without a mantle plume. In
1136 *Special Paper 430: Plates, Plumes and Planetary Processes* (pp. 693-722).
- 1137 King, S. D., & Ritsema, J. (2000). African hot spot volcanism: small-scale convection in the
1138 upper mantle beneath cratons. *Science*, 290(5494), 1137-1140.

- 1139 Korenaga, T., & Korenaga, J. (2016). Evolution of young oceanic lithosphere and the meaning of
1140 seafloor subsidence rate. *Journal of Geophysical Research: Solid Earth*, 121(9), 6315-
1141 6332.
- 1142 Lau, H. C., Austermann, J., Holtzman, B. K., Havlin, C., Lloyd, A. J., Book, C., & Hopper, E.
1143 (2021). Frequency Dependent Mantle Viscoelasticity via the Complex Viscosity: Cases
1144 From Antarctica. *Journal of Geophysical Research: Solid Earth*, 126(11),
1145 e2021JB022622.
- 1146 Lee, C.-T. A. (2003). Compositional variation of density and seismic velocities in natural
1147 peridotites at STP conditions: Implications for seismic imaging of compositional
1148 heterogeneities in the upper mantle. *Journal of Geophysical Research: Solid Earth*,
1149 108(B9).
- 1150 Lee, C.-T. A., Luffi, P., Plank, T., Dalton, H., & Leeman, W. P. (2009). Constraints on the
1151 depths and temperatures of basaltic magma generation on Earth and other terrestrial
1152 planets using new thermobarometers for mafic magmas. *Earth and Planetary Science*
1153 *Letters*, 279(1-2), 20-33. 10.1016/j.epsl.2008.12.020
- 1154 Lei, W., Ruan, Y., Bozdağ, E., Peter, D., Lefebvre, M., Komatitsch, D., et al. (2020). Global
1155 adjoint tomography—model GLAD-M25. *Geophysical Journal International*, 223(1), 1-
1156 21.
- 1157 Lekic, V., Cottaar, S., Dziewonski, A., & Romanowicz, B. (2012). Cluster analysis of global
1158 lower mantle tomography: A new class of structure and implications for chemical
1159 heterogeneity. *Earth and Planetary Science Letters*, 357-358, 68-77.
1160 10.1016/j.epsl.2012.09.014

- 1161 Lynner, C., Delph, J. R., Portner, D. E., Beck, S. L., Sandvol, E., & Ozacar, A. A. Slab induced
1162 mantle upwelling beneath the Anatolian plateau. *Geophysical Research Letters*,
1163 e2021GL097451.
- 1164 Ma, Z., Dalton, C. A., Russell, J. B., Gaherty, J. B., Hirth, G., & Forsyth, D. W. (2020). Shear
1165 attenuation and anelastic mechanisms in the central Pacific upper mantle. *Earth and*
1166 *Planetary Science Letters*, 536, 116148.
- 1167 Madrigal, P., Gazel, E., Flores, K. E., Bizimis, M., & Jicha, B. (2016). Record of massive
1168 upwellings from the Pacific large low shear velocity province. *Nature Communications*,
1169 7(1), 1-12.
- 1170 Marzoli, A., Renne, P. R., Piccirillo, E. M., Ernesto, M., Bellieni, G., & De Min, A. (1999).
1171 Extensive 200-million-year-old continental flood basalts of the Central Atlantic
1172 Magmatic Province. *Science*, 284(5414), 616-618.
- 1173 McKenzie, D. (1984). The generation and compaction of partially molten rock. *Journal of*
1174 *Petrology*, 25(3), 713-765.
- 1175 McNab, F., Ball, P. W., Hoggard, M. J., & White, N. J. (2018). Neogene Uplift and Magmatism
1176 of Anatolia: Insights From Drainage Analysis and Basaltic Geochemistry. *Geochemistry,*
1177 *Geophysics, Geosystems*, 19(1), 175-213. 10.1002/2017gc007251
- 1178 Memiş, C., Göğüş, O. H., Uluocak, E. Ş., Pysklywec, R., Keskin, M., Şengör, A. C., & Topuz,
1179 G. (2020). Long wavelength progressive plateau uplift in Eastern Anatolia since 20 Ma:
1180 implications for the role of slab peel-Back and Break-off. *Geochemistry, Geophysics,*
1181 *Geosystems*, 21(2), e2019GC008726.
- 1182 Morgan, W. J. (1972). Deep mantle convection plumes and plate motions. *AAPG bulletin*, 56(2),
1183 203-213.

- 1184 Moulik, P., & Ekström, G. (2014). An anisotropic shear velocity model of the Earth's mantle
1185 using normal modes, body waves, surface waves and long-period waveforms.
1186 *Geophysical Journal International*, 199(3), 1713-1738.
- 1187 Moussallam, Y., Longpré, M.-A., McCammon, C., Gomez-Ulla, A., Rose-Koga, E. F., Scaillet,
1188 B., et al. (2019). Mantle plumes are oxidised. *Earth and Planetary Science Letters*, 527,
1189 115798.
- 1190 Mundl, A., Touboul, M., Jackson, M. G., Day, J. M., Kurz, M. D., Lekic, V., et al. (2017).
1191 Tungsten-182 heterogeneity in modern ocean island basalts. *Science*, 356(6333), 66-69.
- 1192 Natarov, S. I., & Conrad, C. P. (2012). The role of Poiseuille flow in creating depth-variation of
1193 asthenospheric shear. *Geophysical Journal International*, 190(3), 1297-1310.
- 1194 Nikogosian, I. K., Bracco Gartner, A. J. J., van Bergen, M. J., Mason, P. R. D., & van
1195 Hinsbergen, D. J. J. (2018). Mantle Sources of Recent Anatolian Intraplate Magmatism:
1196 A Regional Plume or Local Tectonic Origin? *Tectonics*, 37(12), 4535-4566.
1197 10.1029/2018TC005219
- 1198 Olson, P. (1990). Hot spots, swells and mantle plumes. In M. P. Ryan (Ed.), *Magma transport*
1199 *and storage* (pp. 33-51). New York: Wiley.
- 1200 Özdemir, Y., Blundy, J., & Güleç, N. (2011). The importance of fractional crystallization and
1201 magma mixing in controlling chemical differentiation at Süphan stratovolcano, eastern
1202 Anatolia, Turkey. *Contributions to Mineralogy and Petrology*, 162(3), 573-597.
- 1203 Parnell-Turner, R., White, N., Henstock, T. J., Jones, S. M., Maclennan, J., & Murton, B. J.
1204 (2017). Causes and consequences of diachronous V-shaped ridges in the North Atlantic
1205 Ocean. *Journal of Geophysical Research: Solid Earth*, 122(11), 8675-8708.

- 1206 Paterson, M., & Olgaard, D. (2000). Rock deformation tests to large shear strains in torsion.
1207 *Journal of structural Geology*, 22(9), 1341-1358.
- 1208 Phipps Morgan, J., Morgan, W. J., Zhang, Y. S., & Smith, W. H. (1995). Observational hints for
1209 a plume-fed, suboceanic asthenosphere and its role in mantle convection. *Journal of*
1210 *Geophysical Research: Solid Earth*, 100(B7), 12753-12767.
- 1211 Plank, T., & Forsyth, D. W. (2016). Thermal structure and melting conditions in the mantle
1212 beneath the Basin and Range province from seismology and petrology. *Geochemistry,*
1213 *Geophysics, Geosystems*, 17(4), 1312-1338. 10.1002/2015gc006205
- 1214 Priestley, K., & McKenzie, D. (2013). The relationship between shear wave velocity,
1215 temperature, attenuation and viscosity in the shallow part of the mantle. *Earth and*
1216 *Planetary Science Letters*, 381, 78-91.
- 1217 Putirka, K. D. (2005). Mantle potential temperatures at Hawaii, Iceland, and the mid-ocean ridge
1218 system, as inferred from olivine phenocrysts: Evidence for thermally driven mantle
1219 plumes. *Geochemistry, Geophysics, Geosystems*, 6(5). 10.1029/2005gc000915
- 1220 Putirka, K. D. (2008). Excess temperatures at ocean islands: Implications for mantle layering and
1221 convection. *Geology*, 36(4), 283-286.
- 1222 Reid, M. R., Schleiffarth, W. K., Cosca, M. A., Delph, J. R., Blichert-Toft, J., & Cooper, K. M.
1223 (2017). Shallow melting of MORB-like mantle under hot continental lithosphere, Central
1224 Anatolia. *Geochemistry, Geophysics, Geosystems*, 18(5), 1866-1888.
1225 10.1002/2016gc006772
- 1226 Rooney, T. O., Hanan, B. B., Graham, D. W., Furman, T., Blichert-Toft, J., & Schilling, J.-G.
1227 (2012). Upper mantle pollution during Afar plume–continental rift interaction. *Journal of*
1228 *Petrology*, 53(2), 365-389.

- 1229 Rudnick, R., Gao, S., Holland, H., & Turekian, K. (2003). Composition of the continental crust.
1230 *The crust*, 3, 1-64.
- 1231 Schoonman, C. M., White, N. J., & Pritchard, D. (2017). Radial viscous fingering of hot
1232 asthenosphere within the Icelandic plume beneath the North Atlantic Ocean. *Earth and*
1233 *Planetary Science Letters*, 468, 51-61. 10.1016/j.epsl.2017.03.036
- 1234 Seton, M., Müller, R. D., Zahirovic, S., Gaina, C., Torsvik, T., Shephard, G., et al. (2012).
1235 Global continental and ocean basin reconstructions since 200 Ma. *Earth-Science Reviews*,
1236 113(3-4), 212-270.
- 1237 Shen, W., & Ritzwoller, M. H. (2016). Crustal and uppermost mantle structure beneath the
1238 United States. *Journal of Geophysical Research: Solid Earth*, 121(6), 4306-4342.
- 1239 Smrekar, S. E., Stofan, E. R., Mueller, N., Treiman, A., Elkins-Tanton, L., Helbert, J., et al.
1240 (2010). Recent hotspot volcanism on Venus from VIRTIS emissivity data. *Science*,
1241 328(5978), 605-608.
- 1242 Stern, T., Lamb, S., Moore, J. D., Okaya, D., & Hochmuth, K. (2020). High mantle seismic P-
1243 wave speeds as a signature for gravitational spreading of superplumes. *Science advances*,
1244 6(22), eaba7118.
- 1245 Stixrude, L., & Lithgow-Bertelloni, C. (2011). Thermodynamics of mantle minerals-II. Phase
1246 equilibria. *Geophysical Journal International*, 184(3), 1180-1213.
- 1247 Trela, J., Gazel, E., Sobolev, A. V., Moore, L., Bizimis, M., Jicha, B., & Batanova, V. G. (2017).
1248 The hottest lavas of the Phanerozoic and the survival of deep Archaean reservoirs. *Nature*
1249 *Geoscience*, 10(6), 451-456. 10.1038/ngeo2954
- 1250 Turcotte, D. L., & Schubert, G. (2002). *Geodynamics*: Cambridge university press.

- 1251 Van Wijk, J., Van Hunen, J., & Goes, S. (2008). Small-scale convection during continental
1252 rifting: Evidence from the Rio Grande rift. *Geology*, *36*(7), 575-578.
- 1253 Vanacore, E. A., Taymaz, T., & Saygin, E. (2013). Moho structure of the Anatolian Plate from
1254 receiver function analysis. *Geophysical Journal International*, *193*(1), 329-337.
1255 10.1093/gji/ggs107
- 1256 Wei, W., Zhao, D., Wei, F., Bai, X., & Xu, J. (2019). Mantle Dynamics of the Eastern
1257 Mediterranean and Middle East: Constraints From P-Wave Anisotropic Tomography.
1258 *Geochemistry, Geophysics, Geosystems*, *20*(10), 4505-4530. 10.1029/2019gc008512
- 1259 Wessel, P., Luis, J., Uieda, L., Scharroo, R., Wobbe, F., Smith, W. H., & Tian, D. (2019). The
1260 generic mapping tools version 6. *Geochemistry, Geophysics, Geosystems*, *20*(11), 5556-
1261 5564.
- 1262 White, W. M. (2020). *Geochemistry*: John Wiley & Sons.
- 1263 Yamauchi, H., & Takei, Y. (2016). Polycrystal anelasticity at near-solidus temperatures. *Journal*
1264 *of Geophysical Research: Solid Earth*, *121*(11), 7790-7820. 10.1002/2016jb013316
- 1265 Yang, A., & Yang, T. (2021). Controls on the present-day dynamic topography predicted from
1266 mantle flow models since 410 Ma. *Geophysical Journal International*, *225*(3), 1637-
1267 1652.
- 1268